

1 **Quantification of primary and secondary organic aerosol**
2 **sources by combined factor analysis of extractive electrospray**
3 **ionisation and aerosol mass spectrometer measurements**
4 **(EESI-TOF and AMS)**

5
6 Yandong Tong^{1,*}, Lu Qi¹, Giulia Stefenelli¹, Dongyu S. Wang¹, Francesco Canonaco¹, Urs
7 Baltensperger¹, André S.H. Prévôt¹, Jay G. Slowik¹

8 ¹Laboratory of Atmospheric Chemistry, Paul Scherrer Institute (PSI), 5232 Villigen,
9 Switzerland

10 *Now at Department of Chemistry, University of Colorado, Boulder, 80310, USA

11 *Correspondence* to Jay Slowik (jay.slowik@psi.ch)

12
13 **Abstract:**

14 **Source apportionment studies have struggled to quantitatively link secondary organic aerosol**
15 **(SOA) to its precursor sources, due largely to instrument limitations. For example, aerosol mass**
16 **spectrometers (AMS) provide quantitative measurements of the total SOA fraction, but lack the**
17 **chemical resolution to resolve most SOA sources. In contrast, instruments based on soft ionisation**
18 **techniques, such as extractive electrospray ionisation mass spectrometry (EESI, e.g., the EESI**
19 **time of flight mass spectrometer, EESI-TOF), have demonstrated the resolution to identify**
20 **specific SOA sources but provide only a semi-quantitative apportionment due to uncertainties in**
21 **the dependence of instrument sensitivity on molecular identity. We address this challenge by**
22 **presenting a method for positive matrix factorisation (PMF) analysis on a single dataset which**
23 **includes measurements from both AMS and EESI-TOF instruments, denoted “combined PMF”**
24 **(cPMF). Because each factor profile includes both AMS and EESI-TOF components, the cPMF**
25 **analysis maintains the source resolution capability of the EESI-TOF, while also providing**
26 **quantitative factor mass concentrations. Therefore, the bulk EESI-TOF sensitivity to each factor**
27 **can also be directly determined from the analysis. We present metrics for ensuring both**
28 **instruments are well-represented in the solution, a method for optionally constraining the profiles**
29 **of factors that are detectable by one or both instruments, and a protocol for uncertainty analysis.**

30
31 **As a proof of concept, the cPMF analysis was applied to summer and winter measurements in**
32 **Zurich, Switzerland. Factors related to biogenic and wood burning-derived SOA are quantified,**
33 **as well as POA sources such as wood burning, cigarette smoke, cooking, and traffic. The retrieved**
34 **EESI-TOF factor-dependent sensitivities are consistent with both laboratory measurements of**
35 **SOA from model precursors and bulk sensitivity parameterisations based on ion chemical**
36 **formulae. The cPMF analysis shows that with the standalone EESI-TOF PMF, in which factor-**
37 **dependent sensitivities are not accounted for, some factors are significantly under/overestimated.**
38 **For example, when factor-dependent sensitivities are not considered in the winter dataset, the**
39 **SOA fraction is underestimated by ~25% due to the high EESI-TOF sensitivity to components of**
40 **primary biomass burning such as levoglucosan. In the summer dataset, where both SOA and total**
41 **OA are dominated by monoterpene oxidation products, the uncorrected EESI-TOF**
42 **underestimates the fraction of daytime SOA relative to nighttime SOA (in which organonitrates**
43 **and less oxygenated C_xH_yO_z molecules are enhanced). Although applied here to an AMS/EESI-**

1 **TOF pairing, cPMF is suitable for the general case of a multi-instrument dataset, thereby**
2 **providing a framework for exploiting semi-quantitative, high-resolution instrumentation for**
3 **quantitative source apportionment.**

4 5 **1. Introduction**

6
7 Atmospheric aerosols negatively affect visibility (Chow et al., 2002), human health (Pope et al., 2002;
8 Laden et al., 2006; Beelen et al., 2014), and urban air quality (Fenger, 1999; Mayer, 1999) on local and
9 regional scales. Aerosols also provide the largest uncertainties for global radiation balance and climate
10 change (Lohmann and Feichter, 2005; Forster et al., 2007; Penner et al., 2011; Myhre et al., 2014).
11 Therefore, to develop appropriate mitigation policies, it is of vital importance to understand aerosol
12 chemical composition, sources, and evolution. Organic aerosol (OA) is a major component of
13 atmospheric aerosol and accounts for 20 to 90 % of the submicron aerosol mass (Jimenez et al., 2009).
14 OA is typically classified as either primary organic aerosol (POA), which is directly emitted to the
15 atmosphere, or secondary organic aerosol (SOA), which is produced by atmospheric reactions of
16 emitted volatile organic compounds (VOCs). Both POA and SOA can exert serious health effects,
17 including protein and DNA damage caused by reactive oxygen species (ROS), which can be either
18 contained in the particles or induced by oxidation reactions following inhalation (Halliwell and Cross,
19 1994; Li et al., 2003; Reuter et al., 2010; Kelly and Fussell, 2012; Fuller et al., 2014). Recent studies
20 indicate that the oxidation potential of SOA is source-dependent. Therefore, different sources likely
21 carry different health risks, highlighting the importance of OA source identification and quantification
22 (Zhou et al., 2018; Daellenbach et al., 2020). Previous studies have been relatively successful in
23 quantitatively linking POA to its sources. However, quantification of SOA sources and/or formation
24 pathways is more challenging due to 1) the chemical complexity of SOA, which can consist of
25 thousands of unique oxidation products, including highly oxygenated molecules and high molecular
26 weight organic oligomers, and 2) limitations of traditional instrumentation for characterising OA
27 chemical composition, especially the SOA fraction. Therefore, the effects of individual SOA sources
28 on health and climate remain poorly constrained.

29
30 Positive matrix factorisation (PMF) is a widely used source apportionment technique. PMF is a bilinear
31 receptor model which represents the measured mass spectral time series as a linear combination of
32 factor mass spectra and their corresponding time-dependent concentrations (Paatero and Tapper, 1994).
33 These factors may then be related to emission sources, and/or atmospheric processes, depending on
34 their chemical and temporal characteristics. PMF has been implemented in extensive online and offline
35 studies worldwide to quantify OA sources. The Aerodyne aerosol mass spectrometer (AMS) is widely
36 used in OA source apportionment studies because it provides online, quantitative measurements of non-
37 refractory PM₁ or PM_{2.5} (particulate matter with aerodynamic diameter smaller than 1 or 2.5 μm ,
38 respectively) chemical composition with high time resolution. Source apportionment studies using PMF
39 based on AMS data have successfully separated and quantified POA sources based on different
40 chemical signatures, e.g., hydrocarbon-like OA (HOA) (Ng et al., 2011b; Zhang et al., 2014; Elser et
41 al., 2016; Sun et al., 2016a; Xu et al., 2019; Zhao et al., 2019), cooking-related OA (COA) (Mohr et al.,
42 2012; Crippa et al., 2013b; Hu et al., 2016; Sun et al., 2016a; Sun et al., 2016b; Xu et al., 2019; Zhao
43 et al., 2019), biomass burning OA (BBOA) (Alfarra et al., 2007; Lanz et al., 2007; Sun et al., 2011),
44 and coal combustion OA (CCOA) (Zhang et al., 2008; Zhang et al., 2014; Elser et al., 2016; Hu et al.,
45 2016; Sun et al., 2016a). However, SOA is typically reported as either a single SOA factor (denoted
46 oxygenated organic aerosol, OOA), or as two factors distinguished by degree of oxygenation (i.e., less
47 oxygenated OOA, LO-OOA, and more oxygenated OOA, MO-OOA) or by volatility (i.e., semi-volatile
48 OOA, SV-OOA, and low-volatility OOA, LV-OOA) (Jimenez et al., 2009; Zhang et al., 2011; Crippa

1 et al., 2013b; Sun et al., 2013; Elser et al., 2016; Sun et al., 2016a; Xu et al., 2019) rather than in terms
2 of sources and/or formation processes. This limitation is due to the vaporisation/ionisation scheme in
3 the AMS, which causes significant thermal decomposition and ionisation-induced fragmentation
4 (DeCarlo et al., 2006). The corresponding decrease in chemical resolution, particularly for
5 multifunctional and/or highly oxygenated SOA components (e.g., multifunctional acids, peroxides,
6 organonitrates, organosulfates, oligomers), limits the resolution of SOA source apportionment.

7
8 The development of continuous or semi-continuous instruments with softer vaporisation/ionisation
9 schemes has provided new insights into SOA composition, and is thus of considerable interest for source
10 apportionment. Recent examples include the (semi-continuous) Filter Inlet for Gases and AEROSols
11 chemical ionisation time-of-flight mass spectrometer (FIGAERO-CIMS) (Lopez-Hilfiker et al., 2014),
12 and the (continuous) extractive electrospray ionisation time-of-flight mass spectrometer (EESI-TOF)
13 (Lopez-Hilfiker et al., 2019), which implement soft ionisation schemes at lower temperatures than the
14 AMS, thereby reducing thermal decomposition and increasing chemical resolution (i.e., providing
15 chemical formulae of molecular ions). A recent source apportionment study using a FIGAERO-CIMS
16 at a rural site in the southeastern USA successfully resolved three SOA factors, characterised by
17 isoprene-derived species such as carboxylic acids from aqueous phase processes, highlighting the
18 chemistry of biogenic species (Chen et al., 2020). Another source apportionment study from Lee et al.
19 (2020) using FIGAERO-CIMS spectra successfully distinguished ambient SOA formation and ageing
20 pathways in two forested regions. Source apportionment studies in Zurich using an EESI-TOF identified
21 SOA factors from monoterpene oxidation in summer (Stefenelli et al., 2019) and oxidation of biomass
22 burning emissions in winter (Qi et al., 2019). EESI-TOF measurements identified SOA factors related
23 to solid fuel combustion and aqueous-phase processes in Beijing (Tong et al., 2021) and SOA factors
24 with aromatic and biogenic origins in Delhi (Kumar et al., 2021). However, to date the factor
25 concentrations returned by PMF analyses using these instruments are not quantitative.

26
27 Quantification of the measurements by instruments such as EESI-TOF and CIMS is challenging
28 because the instrument sensitivity varies strongly with molecular identity. For CIMS, the sensitivity to
29 different compounds is determined by the frequency of collisions between reagent ions and analytes,
30 the ion–molecule reaction time, and the transmission efficiency of product ions to the detector, which
31 depends on ion-molecule binding energy. Lopez-Hilfiker et al. (2016) developed methods to estimate
32 the binding energy of iodide (I⁻) adduct ions of multifunctional organic compounds for species whose
33 formation is collision-limited, providing a lower limit to their mass concentrations. Another method to
34 explore the sensitivity is to measure single-compound aerosols or SOA generated from different
35 precursors simultaneously by an EESI-TOF and a scanning mobility particle sizer (SMPS) to determine
36 the mass concentration (Lopez-Hilfiker et al., 2016). Lopez-Hilfiker et al. (2019) explored EESI-TOF
37 sensitivities to selected reference compounds with different functional groups (including saccharides,
38 polyols and carboxylic acids) and bulk SOA generated from oxidation of a single precursor VOC. For
39 pure compounds, relative sensitivities vary by two orders of magnitude, with some composition-
40 dependent trends evident (e.g., increasing sensitivity of saccharides with decreasing molecular weight,
41 and high sensitivities for polyols relative to other functionalities). In addition, a trend of decreasing
42 sensitivity with decreasing molecular weight of the precursors was found for bulk SOA. While
43 calibration with standard compounds is straightforward, the quantification of individual species within
44 SOA is extremely challenging, due to its complex composition, the lack of chemical standards for most
45 molecules, and the potential for structural isomers to have significantly different sensitivities. These
46 issues were investigated recently for the EESI-TOF by generating SOA in the presence of a variable
47 seed surface area, and comparing the difference in SOA ion concentrations measured by the EESI-TOF
48 and the corresponding gas-phase concentrations measured by a Vocus proton transfer reaction-mass

1 spectrometer (Vocus-PTR-MS) (Wang et al., 2021). The observed sensitivities for different SOA
2 components produced from the oxidation of limonene, *o*-cresol, or 1,3,5-trimethylbenzene ranged from
3 10^3 to 10^5 ion s^{-1} ppb $^{-1}$. A regression model was developed that was able to predict the ion-by-ion
4 sensitivities to within a factor of 5 of the experimental value when the precursor VOC is known *a priori*.
5 However, the study also showed significantly different sensitivities (up to a factor of 20) for structural
6 isomers derived from different VOC precursors. Similar isomer sensitivity differences for the I-CIMS
7 were also reported by (Bi et al., 2021). The fact that these isomers cannot be distinguished by 1-
8 dimensional mass spectrometry, represents a fundamental limitation of calibration/parameterisation-
9 based quantification and complicates interpretation of the binding energy-based approach (Lopez-
10 Hilfiker et al., 2016), because ambient SOA may derive from unknown or complex mixtures of VOCs.
11 Therefore, for source apportionment purposes, source-based sensitivities are preferred and essential to
12 quantify SOA sources and formation processes.

13

14 Here we present a new approach for quantification of SOA sources retrieved from source apportionment.
15 This is achieved by PMF analysis of a single input matrix consisting of data from both a quantitative
16 instrument with lower chemical resolution (i.e., AMS) and an instrument with high chemical resolution
17 and a linear but molecule-dependent response (i.e., EESI-TOF). This method is based on the combined
18 PMF (cPMF) analysis previously performed on combined OA/VOC data from AMS and PTR-MS,
19 respectively (Slowik et al., 2010; Crippa et al., 2013a), but utilises a more robust metric for ensuring
20 adequate representation of both instruments in the model solution, optionally allows constraints to be
21 placed on the factor profile contributions for one or both instruments, and provides a method for
22 uncertainty analysis. The cPMF method is applied to AMS/EESI-TOF datasets collected during summer
23 and winter campaigns in Zurich, Switzerland, for which single-instrument PMF analyses were
24 previously reported (Qi et al., 2019; Stefanelli et al., 2019). The present study is the first application of
25 cPMF to a joint EESI-TOF/AMS dataset, and the first quantitative EESI-TOF-driven source
26 apportionment.

27

28 **2. Methodologies**

29

30 **2.1 The measurement site and field campaigns**

31

32 Field campaigns were conducted at the Swiss National Air Pollution Monitoring Network (NABEL)
33 station, an urban background site located in the Alte Kaserne, central Zurich (47°22' N, 8°33' E, 410 m
34 above sea level), previously described in detail (Lanz et al., 2007; Canonaco et al., 2013). The
35 measurements used in the current analysis are from 20 June to 26 June 2016 and 25 January to 4
36 February 2017. These periods are excerpted from longer campaigns, and correspond to the times during
37 which both the AMS and EESI-TOF achieved stable operation. The measurement site is located in a
38 courtyard, although influences from nearby restaurants, local minor roads, and human activities (e.g.,
39 cigarette smoking) are often observed (Lanz et al., 2007; Daellenbach et al., 2017; Qi et al., 2019;
40 Stefanelli et al., 2019; Qi et al., 2020). Gas-phase species, e.g., nitrogen dioxide (NO₂), nitrogen oxide
41 (NO) and sulfur dioxide (SO₂) and meteorological data, e.g., temperature (T), relative humidity (RH),
42 radiation, wind speed (WS) and wind direction (WD) are recorded by the monitoring station.

41

42 During the intensive campaigns, a separate trailer was deployed to house an additional suite of gas and
43 particle instrumentation. A PM_{2.5} cyclone was installed ~75 cm above the trailer roof (~5 m above
44 ground) to remove coarse particles. After passing through the cyclone, the sampled air passed through
45 a stainless steel (~6 mm outer diameter, O.D.) tube to the particle instrumentation, which included a
46 high-resolution time-of-flight aerosol mass spectrometer (HR-TOF-AMS, Aerodyne Research Inc.) and
47 an extractive electrospray ionisation time-of-flight mass spectrometer (EESI-TOF) to measure the OA
48 composition, and a scanning mobility particle sizer (SMPS) to measure the particle concentration and

1 size distribution. The summer and winter campaign results, including OA source apportionment from
2 the standalone AMS and EESI-TOF datasets, were previously presented in detail (Qi et al., 2019;
3 Stefenelli et al., 2019). In this study, we focus on the OA source apportionment using positive matrix
4 factorisation (PMF) on the combined dataset from AMS and EESI-TOF, collected during the two
5 campaigns.

6 **2.2 Instrumentation**

7 2.2.1 High-resolution time-of-flight aerosol mass spectrometer (HR-TOF-AMS)

8
9
10 The AMS (Aerodyne Research, Inc.) provides fast, online, quantitative measurements of the size-
11 resolved composition of non-refractory PM₁ (NR-PM₁). A detailed description of the instrument can be
12 found elsewhere (DeCarlo et al., 2006; Canagaratna et al., 2007), while operational details and data
13 treatment are documented in Stefenelli et al. (2019) and Qi et al. (2019). Briefly, in both campaigns,
14 the organic composition of NR-PM₁ was measured by AMS with a time resolution of 1 min. At the
15 beginning and end of the both campaigns, the instrument was calibrated for ionisation efficiency (IE)
16 using 400 nm NH₄NO₃ particles using the mass-based method (Jimenez et al., 2003; Canagaratna et al.,
17 2007). The HR-TOF-AMS data was analysed using the SQUIRREL (v.1.57) and PIKA (v.1.16)
18 software packages in IGOR Pro 6.37 (Wavemetrics, Inc., Portland, OR, USA). Before further single-
19 instrument and cPMF analysis, a composition-dependent collection efficiency (CDCE) was
20 implemented to correct the measured aerosol mass (Middlebrook et al., 2012). For both single-
21 instrument PMF and cPMF analysis, the input matrices consisted of the time series of fitted OA ions
22 from high-resolution mass spectral analysis, together with their corresponding uncertainties estimated
23 from ion counting statistics and detector variability according to Allan et al. (2003). Following Ulbrich
24 et al. (2009), a minimum error value was applied to the error matrix. Ions with signal-to-noise ratio
25 (SNR) smaller than 0.2 were excluded in the further analysis, whereas ions with an SNR between 0.2
26 and 2 were downweighted by a factor of 2 (Paatero and Hopke, 2003). The contribution of nitrate ions
27 to CO₂⁺ was estimated separately in each campaign from their respective NH₄NO₃ calibrations (Pieber
28 et al., 2016).

29
30 The AMS PMF input matrices are identical to those used by Stefenelli et al. (2019) and Qi et al. (2019),
31 with the exception that they include not only the OA ions retrieved from spectral analysis, but also NO⁺
32 and NO₂⁺. These ions are added because they represent the major products measured from organonitrate
33 fragmentation (Farmer et al., 2010), and standalone EESI-TOF PMF suggested a significant role for
34 organonitrates and other nitrogen-containing species during both the summer and winter campaigns (Qi
35 et al., 2019; Stefenelli et al., 2019). Detailed descriptions of the final input matrices from AMS (e.g.,
36 number of measurements, number of ions and time resolution) in summer and in winter are presented
37 in Table 1.

38 2.2.2 Extractive electrospray ionisation time-of-flight mass spectrometer (EESI-TOF)

39
40
41 The EESI-TOF provides online, fast, near-molecular-level measurement (i.e., chemical formulae of
42 molecular ions) of OA composition, without thermal decomposition or ionisation-induced
43 fragmentation. A detailed description can be found elsewhere (Lopez-Hilfiker et al., 2019) and the
44 operational details for the summer and winter campaigns are documented in Stefenelli et al. (2019) and
45 Qi et al. (2019), respectively. Briefly, aerosol particles were continuously sampled through a 6 mm
46 O.D., 5 cm long multi-channel extruded carbon denuder. Particles then intersected a spray of charged
47 droplets generated by a conventional electrospray probe and the soluble fraction was extracted into the
48 droplets. The droplets passed through a heated stainless-steel capillary (~250 °C), wherein the

1 electrospray solvent evaporated, and ions were ejected into the mass spectrometer. Due to the short
 2 residence time (~ 1 ms) in the capillary, no thermal decomposition was observed. The analyte ions were
 3 detected by a high-resolution time-of-flight mass spectrometer with an atmospheric pressure interface
 4 (API-TOF) (Junninen et al., 2010). In the summer campaign, the electrospray consisted of a 1:1
 5 water/methanol (MeOH, UHPLC-MS grade, LiChrosolv) mixture doped with 100 ppm NaI ($>99\%$,
 6 Sigma-Aldrich). In the winter campaign, a 1:1 water/acetonitrile mixture ($>99.9\%$, Sigma-Aldrich)
 7 mixture with 100 ppm NaI (99% , Sigma-Aldrich) was utilised, which reduced background signal. In
 8 both campaigns, the mass spectrometer was configured to detect positive ions. Because of NaI use,
 9 analyte ions were detected almost exclusively as $[M]Na^+$ and other ionisation pathways were suppressed
 10 (the only notable exception being nicotine, which was detected as $[C_{10}H_{14}N_2]H^+$). This yields a linear
 11 response to mass, avoids matrix effects, and simplifies spectral interpretation (Lopez-Hilfiker et al.,
 12 2019). Adducts of an analyte with acetonitrile or methanol molecule(s) may also be detected by the
 13 instrument, depending on the voltage settings in the ion transfer optics (i.e., collision energy), but these
 14 adducts were observed to have negligible signals with our voltage configurations in both campaigns.
 15 The EESI-TOF alternates between direct sampling (8 min) and sampling through a particle filter (3 min)
 16 to provide a measurement of instrument background (including spray). No major changes between
 17 adjacent background measurements were observed in either campaign (Qi et al., 2019; Stefenelli et al.,
 18 2019).

19
 20 Data analysis, including high-resolution peak fitting, was performed using Tofware version 2.5.7
 21 (Tofwerk AG, Thun, Switzerland). Detailed data treatment processes can be found in Stefenelli et al.
 22 (2019) and Qi et al. (2019). The EESI-TOF alternates between periods of direct ambient sampling (M_{amb})
 23 and filter sampling (M_{bkgd}), with the filter periods interpolated to yield an estimated background
 24 spectrum during ambient measurements ($M_{bkgd,est}$). The spectra corresponding to aerosol composition
 25 (M_{diff}) are determined by the difference of M_{amb} and $M_{bkgd,est}$ as shown in Eq. (1a). The corresponding
 26 error matrix was estimated by adding in quadrature the uncertainties of the total sampling measurement
 27 $s_{amb}(i,j)$ and the filter sampling measurement $s_{bkgd,est}(i,j)$ as shown in Eq. (1b), which are in turn
 28 calculated from ion counting statistics and detector variability (Allan et al., 2003):

$$30 \quad M_{diff}(i,j) = M_{amb}(i,j) - M_{bkgd,est}(i,j) \quad (1a)$$

$$31 \quad s_{diff}(i,j) = \sqrt{s_{amb}^2(i,j) + s_{bkgd,est}^2(i,j)} \quad (1b)$$

32 where the unit of all quantities in both equations is counts per second (cps). Ions with a mean SNR
 33 smaller than 2 were removed from both matrices, because the signals of these ions were predominantly
 34 caused by electrospray and/or instrumental background. Input matrix dimensions are summarised in
 35 Table 1.

36
 37 In theory, EESI-TOF signal for an ion x can be converted from ion flux (cps) to mass concentration
 38 ($\mu\text{g m}^{-3}$), according to Eq. (2):

$$39 \quad Mass_x = I_x \cdot \frac{MW_x}{EE_x + CE_x + IE_x + TE_{m/z}} \cdot \frac{1}{F} \quad (2)$$

40
 41 where $Mass_x$ and I_x are the mass concentration (in $\mu\text{g m}^{-3}$), and the ion flux (cps) reaching the detector
 42 for an ion x , respectively. MW_x represents the molecular weight of the measured ion (e.g., $[M]Na^+$)
 43 (Lopez-Hilfiker et al., 2019; Qi et al., 2019; Stefenelli et al., 2019). EE_x , CE_x , IE_x and $TE_{m/z}$ denote
 44 EESI extraction efficiency (the probability that a molecule dissolves in the spray), EESI collection
 45 efficiency (the probability that the analyte-laden droplet enters the inlet capillary), ionisation efficiency

1 (the probability that an ion forms and subsequently survives declustering forces induced by evaporation
 2 and electric fields), and ion transmission efficiency (the probability that a generated ion is transmitted
 3 to the detector, which is independent from chemical identity but depends only on m/z), respectively. F
 4 indicates the flow rate. In practice, several of these parameters are ion-dependent and remain
 5 uncharacterised, and therefore conversion to mass concentration on an ion-by-ion basis cannot currently
 6 be achieved (Lopez-Hilfiker et al., 2019). Instead, to facilitate comparison with bulk quantities, we
 7 define an “apparent sensitivity (AS)” to describe the EESI-TOF response to a measured concentration
 8 of species x , as shown in Eq. (3):

$$AS_x = \frac{MW_x}{EE_x \cdot CE_x \cdot IE_x \cdot TE_{m/z}} \cdot \frac{1}{F} = \frac{I_x}{Mass_x} \quad (3)$$

9 where I_x is the measured ion flux (counts per second, cps) for the ion or factor x detected by EESI-TOF,
 10 $Mass_x$ is measured mass concentration ($\mu\text{g m}^{-3}$) from a reference instrument for the same ion or factor
 11 x , thus the AS is in the unit of cps ($\mu\text{g m}^{-3}$)⁻¹. Equation (3) is used to determine the apparent factor-
 12 specific sensitivities from cPMF outputs by defining the AMS contribution to the factor profile ($\mu\text{g m}^{-3}$)
 13 as $Mass_x$ and the EESI-TOF contribution (cps) as I_x .

14 2.2.3 Estimation of EESI-TOF sensitivities from a multi-variate model

15
 16 For comparison to the factor-dependent sensitivities determined by the cPMF analysis (Eq. 3), we also
 17 estimated sensitivities for SOA factors from molecular formulae of individual analyte ions using
 18 parameterisations developed from laboratory measurements of SOA generated from oxidation of
 19 limonene (LMN) by ozone and *o*-cresol (cresol) and 1,3,5-trimethylbenzene (TMB) by OH radicals
 20 (Wang et al., 2021). As discussed in Sect. 1, the parameterisation can predict the relative sensitivities
 21 of ions measured by the EESI-TOF to within a factor of 5, provided that the SOA is derived from a
 22 single, known VOC. However, for ambient data, SOA derives from multiple precursor VOCs,
 23 increasing uncertainties. For example, SOA isomers generated from different precursors can differ by
 24 up to a factor of 20 in relative sensitivity (Wang et al., 2021). This represents a significant source of
 25 uncertainty for calibration/parameterisation-based approaches for quantifying SOA factors from source
 26 apportionment but is nonetheless a useful point of comparison.

27
 28 In the present study, we utilise a well-performing model from Wang et al. (2021), namely the gradient
 29 boosting regression, denoted GBR, developed in scikit-learn packages in Spyder 4.1.4 and Python 3.8.3.
 30 The SOA parameterisation derived from LMN was used to predict the sensitivities for summer SOAs
 31 (which are predominantly terpene-derived SOAs), and SOA systems derived from cresol and TMB
 32 were used to predict the sensitivities for winter SOAs (which are characterised by aromatics from
 33 biomass burning activities). The regression models provide compound-dependent relative sensitivities
 34 (AS_x) based only on molecular formulae. Then, the EESI-TOF signals for each factor are calculated as
 35 a signal-weighted average from the respective factor profiles, as shown in Eq. (4):
 36

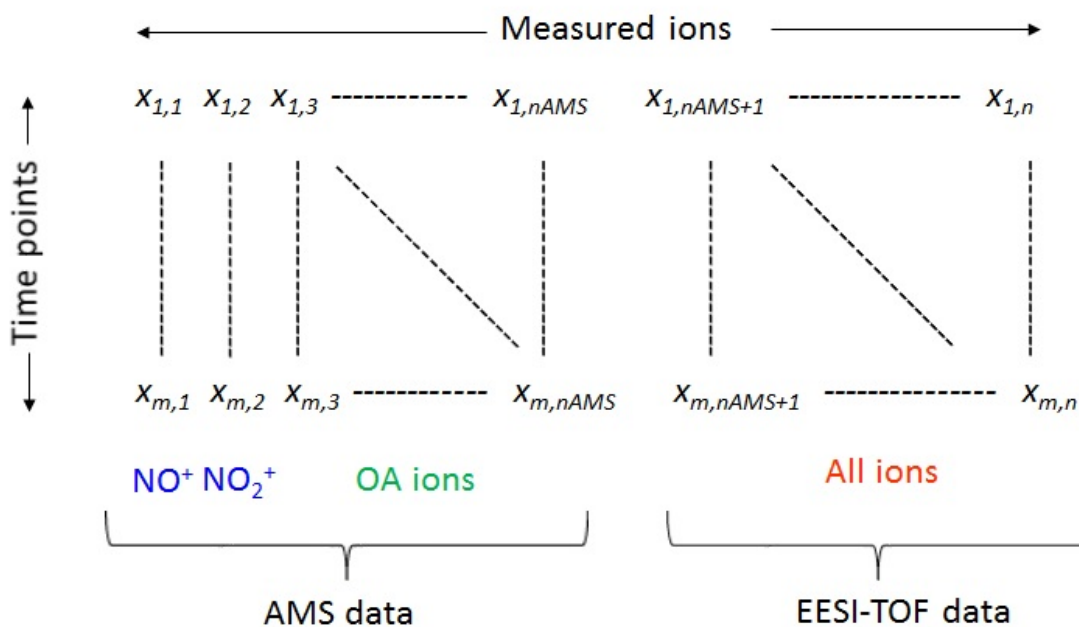
$$AS_{factor} = \frac{\sum_x I_x}{\sum_x (I_x / AS_x)} \quad (4)$$

37
 38 Here I_x denotes the contribution to the factor profile of each ion x . Because the model parameterisations
 39 are based on laboratory SOA that contained only the CHO group, while the resolved OA sources in this
 40 study include both CHO and CHON, we approximate the total factor sensitivity by assuming the
 41 average EESI-TOF sensitivity to CHON ions is equal to the average sensitivity of CHO ions (on a
 42 factor-by-factor basis). Note that the ions from the CHO group contribute a major fraction in SOA mass
 43 for each factor, comprising 85.2 %, 78.1 %, 57.3 % and 76.3 % for DaySOA1, DaySOA2, NightSOA1

1 and NightSOA2 for summer and 77.9 % and 75.0 % to SOA1 and SOA2 for winter, reducing the
 2 uncertainties introduced by this assumption. The factor-specific sensitivities derived from cPMF (Eq.
 3 3) and from the GBR model (Eq. 4) are compared in Sect. 3.2.

6 2.3 Combined Positive Matrix Factorisation (cPMF) Method

8 The source apportionment model used in this study is based on positive matrix factorisation (PMF),
 9 which is widely used in the environmental studies. PMF is a bilinear receptor factor analysis model that
 10 decomposes time series of measured variables (here related to particle composition) into factor
 11 contributions and factor profiles. Different from conventional PMF analysis, which is typically
 12 conducted on a dataset collected by a single instrument, here PMF is applied to a single input dataset
 13 containing both AMS and EESI-TOF mass spectral data. A conceptual schematic of the input data
 14 matrix is shown in Fig. 1. Herein we denote the overall method governing analysis of such a merged
 15 dataset as “combined PMF” (cPMF), while “PMF” denotes both the general PMF model and single-run
 16 executions by the Multilinear Engine solver (see Sect. 2.3.0), which are identical for PMF and cPMF.



18
 19 Figure 1. Schematic of the combined EESI-TOF and AMS input data matrix (X) for cPMF. Matrix
 20 dimensions for the summer and winter datasets are provided in Table 1.

21
 22 This section presents an overview of the cPMF method, with detailed descriptions of each step in the
 23 referenced sub-sections. In the Text S2 in the Supplement, we present details of its application to the
 24 test datasets, including dataset-specific decisions (e.g., which factors to constrain, criteria for
 25 accepting/rejecting solutions) required during certain steps. The overall procedure is outlined in Fig. 2,
 26 with the main steps as follows:

- 27 0) PMF analyses are conducted on the standalone EESI-TOF and AMS datasets with synchronised
 28 time resolution, including constraints on factor profiles as necessary. Residual distributions
 29 from the optimised solutions are used later in step 3 as a criterion for assessing relative
 30 instrument weight.

- 1) The EESI-TOF and AMS datasets with synchronised time resolution are combined into a single input matrix. This input matrix contains OA spectra from EESI-TOF and AMS, as well as the NO^+ and NO_2^+ ions measured by the AMS due to the contributions of organonitrates to these ions (Sect. 2.3.1).
- 2) For any factors that are to be constrained, joint AMS/EESI-TOF profiles are constructed (Sect. 2.3.2 and Text S2.2).
- 3) An exploratory PMF analysis is conducted on the joint AMS/EESI-TOF matrix. This consists of a 2-D exploration of the solution space defined by the number of factors (p) and relative instrument weight (C) (Sect. 2.3.3). The instrument weight ensures that both instruments are well-represented in the solution and is assessed by comparing residuals from cPMF and standalone PMF. For computational efficiency, the profiles of all constrained factors are not allowed to deviate from their reference profiles. Solutions in which both instruments receive approximately equal weight are evaluated for environmental interpretability, with the most interpretable solution utilised as the base case for further analysis. Note that the base case is fully defined by C , p , and the set of constrained factor profiles.
- 4) From the selected base case, 1000 PMF runs are conducted, which combine bootstrap analysis with random selection of a values (i.e., tightness of constraint) for the constrained factors within predetermined limits that are defined on a factor-by-factor basis (Sect. 2.3.4). This requires the following as prerequisites:
 - a. Definition of dataset-specific criteria for acceptance/rejection of individual runs (Text S2.4).
 - b. Determination of the a value range on a factor-by-factor basis giving a reasonable acceptance probability, i.e., sufficient rejection rate to ensure adequate exploration while maintaining computational efficiency (Text S2.4).

The final cPMF result is taken as the mean of all accepted solutions from the bootstrap/ a -value analysis, with uncertainties represented by the standard deviation. From this mean solution, quantitative time series and EESI-TOF factor-specific sensitivities are calculated.

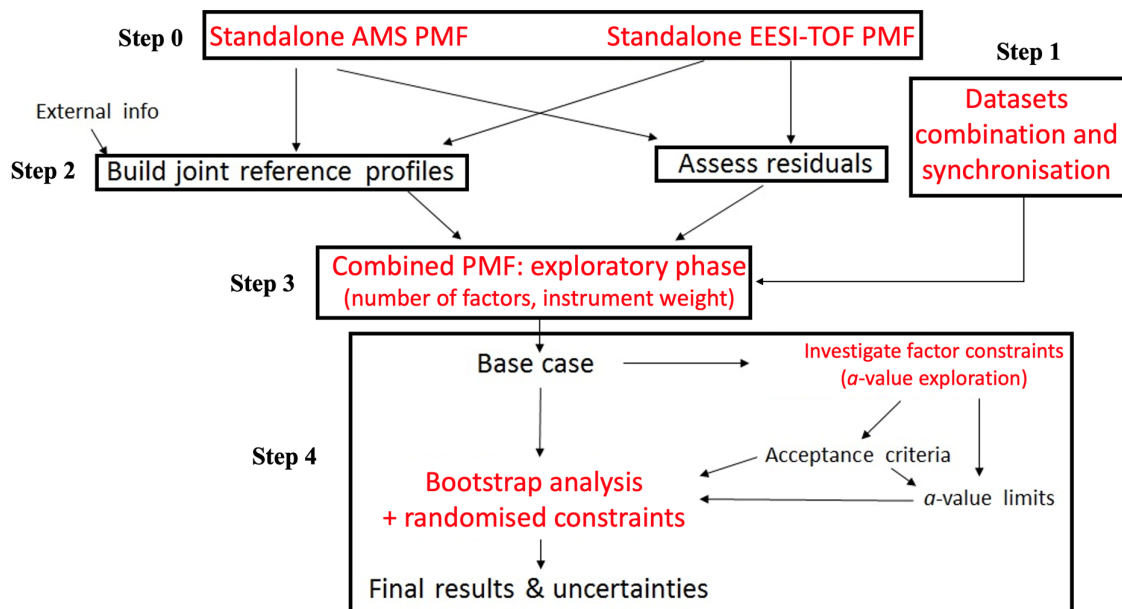


Figure 2. Flow chart summary of cPMF analysis workflow. Red text denotes PMF model operations while black text denotes inputs, outputs, and/or analysis decisions.

2.3.0 Positive matrix factorisation (PMF) principles

In this step, PMF analyses are conducted on the standalone EESI-TOF and AMS datasets with synchronised time resolution, including constraints on factor profiles as necessary. Residuals from these

1 solutions are used to derive as a reference quantity to retrieve a balanced solution (procedure described
 2 in step 3). This step is a parallel step and a preparation for the cPMF, therefore, we denote this step as
 3 step 0.

4
 5 Positive matrix factorisation (PMF) is implemented using the Multilinear Engine (ME-2) (Paatero,
 6 1999), with model configuration and post-analysis performed with the Source Finder (SoFi, version 6B)
 7 (Canonaco et al., 2013), programmed in Igor Pro 6.39 (Wavemetrics, Inc.). PMF is a bilinear receptor
 8 model, which operates on an input data matrix \mathbf{X} (here the mass spectral time series collected by EESI-
 9 TOF and/or AMS) and uncertainty matrix \mathbf{S} , which corresponds point-by-point to \mathbf{X} . PMF describes \mathbf{X}
 10 as a linear combination of static factor profiles (in this case characteristic mass spectra, representing
 11 specific sources and/or atmospheric processes) and their corresponding time-dependent source
 12 contributions, as described in Eq. (5):

$$13 \quad \mathbf{X} = \mathbf{G} \times \mathbf{F} + \mathbf{E} \quad (5)$$

14
 15 Here \mathbf{X} has dimensions of $m \times n$, representing m measurements of n variables (here ions), \mathbf{G} and \mathbf{F} are
 16 respectively the factor time series with the dimension of $m \times p$, and factor profiles with the dimension of
 17 $p \times n$, where p is the number of factors in the PMF solution, and is determined by the user. \mathbf{E} is the
 18 residual matrix and defined by Eq. (5). The corresponding uncertainty matrix \mathbf{S} and residual matrix \mathbf{E}
 19 are constructed in the same way (Slowik et al., 2010). Note that the AMS component of \mathbf{X} , \mathbf{S} and \mathbf{E} is
 20 in $\mu\text{g m}^{-3}$, and the EESI-TOF component is in cps. Also, \mathbf{X} includes not only organic ions from the
 21 AMS, but also NO^+ and NO_2^+ , which contain a large fraction of the AMS signal derived from
 22 organonitrates (Farmer et al., 2010).

23
 24 Equation (5) is solved by a least-squares algorithm that iteratively minimises the quantity Q , which is
 25 defined in Eq. (6) as the sum of the squares of the uncertainty-weighted residuals:

$$26 \quad Q = \sum_i \sum_j \left(\frac{e_{ij}}{s_{ij}} \right)^2 \quad (6)$$

27
 28 Here e_{ij} is an element in the residual matrix \mathbf{E} , and s_{ij} is the corresponding element in the uncertainty
 29 matrix, where i and j are the indices representing time and ion (or m/z), respectively.

30
 31 However, different combinations of the \mathbf{G} and \mathbf{F} matrices may result in solutions with the same or
 32 similar Q (rotational ambiguity), which in practice leads to mixed or unresolvable factors. Here we
 33 explore a subset of the possible PMF/cPMF solutions in which one or more factor profiles are
 34 constrained using the a -value approach to direct solutions towards environmentally meaningful
 35 rotations. These factors are constrained using reference profiles, with the scalar a ($0 \leq a \leq 1$) determining
 36 the tightness of constraint as follows:

$$37 \quad (f_{k,j})_{\text{sol}} = (f_{k,j})_{\text{ref}} \pm a \times (f_{k,j})_{\text{ref}} \quad (7)$$

38
 39 Here $(f_{k,j})_{\text{ref}}$ represents the reference profile and $(f_{k,j})_{\text{sol}}$ the final profile returned by the model. Due
 40 to the renormalisation of matrices after PMF runs, the final values in $(f_{k,j})_{\text{sol}}$ may slightly exceed the
 41 prescribed range. This approach has been shown to significantly improve the model performance
 42 relative to unconstrained PMF (Canonaco et al., 2013; Crippa et al., 2014; Daellenbach et al., 2016; Qi
 43 et al., 2019; Stefenelli et al., 2019).

1 Due to the nature of the cPMF \mathbf{X} matrix, each retrieved factor has a single time series, which can be
 2 expressed in the concentration units of either instrument, and the factor profile contains both an AMS
 3 and an EESI-TOF component. The factor time series for a single factor k is calculated as follows:

$$4 \quad (g_{i,k})_{inst} = g_{i,k} \cdot \sum_{j=inst} f_{k,j} \quad (8)$$

5
 6 Here $(g_{i,k})_{inst}$ refers generally to the time series in the measurement units of a given instrument, which
 7 we denote $(g_{i,k})_{AMS}$ or $(g_{i,k})_{EESI}$, and the $j=inst$ formalism denotes the set of ions measured by the
 8 respective instrument. For ease of interpretation, we report the instrument contribution to each factor
 9 profile as the mass spectrum (in the respective instrument units) that would be obtained for a factor
 10 mass concentration of $1 \mu\text{g m}^{-3}$. This is expressed as follows, for a single factor k :

$$11 \quad (f_{k,j})_{inst} = \left(\frac{\overline{f_{k,j}(g_{i,k})_{AMS}}}{g_0} \right)_{j=inst} \quad (9)$$

12
 13 Here $\overline{(g_{i,k})_{AMS}}$ denotes the mean of the factor time series in AMS units ($\mu\text{g m}^{-3}$), g_0 is a reference mass
 14 concentration (chosen here as $1 \mu\text{g m}^{-3}$), the $j=inst$ formulation again refers to all ions measured by a
 15 given instrument. We refer to the organic fraction of AMS profile components and EESI-TOF profile
 16 components as $(f_{k,j})_{AMS}$ and $(f_{k,j})_{EESI}$, respectively. The EESI-TOF apparent sensitivity (AS_x , defined
 17 in Eq. (3)) can then be calculated for a single factor k as:

$$18 \quad AS_k = \left(\frac{\overline{(g_{i,k})_{EESI}}}{\overline{(g_{i,k})_{AMS}}} \right)_{j=inst} \quad (10)$$

19
 20 Evaluation of factor interpretability for PMF analysis of the data from a single instrument typically
 21 includes: 1) correlation of the time series with external data; 2) comparison of factor diurnal cycles with
 22 known source activity and previous measurements; 3) identification of source-specific spectral features.
 23 In addition to these three points, factors from cPMF were also interpreted by considering the consistency
 24 of spectral features between the AMS and EESI-TOF, e.g., factors originated from fresh biomass
 25 burning activities are characterised by elevated signal from $\text{C}_2\text{H}_4\text{O}_2^+$ in the AMS spectrum and
 26 levoglucosan in the EESI-TOF spectrum.

27 28 2.3.1 Dataset combination and synchronisation

29
 30 In this step, the time resolution of the EESI-TOF and AMS are synchronised and the datasets with
 31 overlap temporal coverage are combined into a single input matrix, as shown in Fig. 1. This input matrix
 32 contains OA spectra from EESI-TOF and AMS, as well as the NO^+ and NO_2^+ ions measured by the
 33 AMS due to the contributions of organonitrates to these ions. The corresponding error matrix is also
 34 constructed in the same way.

35 36 2.3.2 Constraints on factor profiles

37
 38
 39 If one or more factors are constrained in the Sect. 2.3.0, these factors should also be constrained in this
 40 step, in which the principle of a -value approach in Eq. (7) applies here too. In the cPMF, it may be
 41 desirable to constrain a factor for which a single reference profile incorporating both AMS and EESI-

1 TOF mass spectra is not available. For example, a factor may be detectable by only one instrument, or
 2 reference profiles may have been retrieved independently for each instrument (e.g., from different
 3 studies). In such cases, the cPMF reference profile, $(f_{k,j})_{j=all,ref}$ is constructed from merged
 4 individual profiles as follows:

$$6 \quad \frac{(f_{k,j})_{j=all,ref}}{1 \mu\text{g m}^{-3}} = \begin{cases} \frac{(f_{k,j})_j}{\sum_j (f_{k,j})_j}, & j \in AMS,ref \\ AS_k \cdot \frac{(f_{k,j})_j}{\sum_j (f_{k,j})_j}, & j \in EESI,ref \end{cases} \quad (11)$$

7
 8
 9 Here $(f_{k,j})_j$ denotes standalone reference profiles for the AMS and EESI-TOF, respectively. Note that
 10 although Eq. (11) requires an initial value of AS_k to be assumed prior to PMF execution and utilised
 11 during the exploratory phase of cPMF (Sect. 2.3, step 3), selection of a non-zero a value during
 12 bootstrap analysis (Sect. 2.3, step 4) allows the final AS_k to be determined by the algorithm within the
 13 designated boundaries. Therefore, only a reasonable *a priori* estimate is required. In the case that a
 14 factor is undetectable by the EESI-TOF (e.g., non-oxygenated hydrocarbons comprising traffic-related
 15 factors), a value of AS_k is assumed that fixes the EESI-TOF contribution near zero, as discussed in the
 16 Supplement in Text S1. In the present study, we utilised $AS_k = 0.01 \text{ cps } (\mu\text{g m}^{-3})^{-1}$ when this situation
 17 arose (e.g., HOA and InorgNit reference profiles are constructed using this method). For contrast, AS_k
 18 for factors detectable by both instruments ranged from approximately 100 to 1000 $\text{cps } (\mu\text{g m}^{-3})^{-1}$.

20 2.3.3 Exploratory phase of cPMF

21 In this step, an exploratory PMF analysis is conducted on the joint AMS/EESI-TOF matrix. This
 22 consists of a 2-D exploration of the solution space defined by the number of factors (p) and relative
 23 instrument weight (C). For both factor interpretation and quantitative analysis, it is important that both
 24 instruments be well-represented in any accepted PMF solution. In principle, the extent to which PMF
 25 can explain a variable $x_{i,j}$ is limited by the measurement uncertainty, $s_{i,j}$; that is, the expectation value
 26 of the scaled residual ($e_{i,j}/s_{i,j}$) is 1 (i.e., $Q/Q_{expect} \sim 1$). In practice, $e_{i,j}/s_{i,j}$ may be systematically above or
 27 below 1, and differ between instruments, for several reasons. First, the accuracy of the error calculation
 28 may be systematically different between instruments, leading to systematic differences in the effect of
 29 residuals from a given instrument on Q . Second, the extent of internal correlations in the dataset may
 30 differ between instruments. For example, fragmentation/thermal decomposition in the AMS can lead to
 31 sequences of correlated ions (e.g., $\text{C}_n\text{H}_{2n+1}^+$ for alkanes). In contrast, for the EESI-TOF measurement of
 32 individual molecular ions, ion-to-ion correlations depend solely on particle composition. Finally, even
 33 for a case where ion-by-ion signal-to-noise and the extent of internal correlations is equal between
 34 instruments, the relative number of variables (ions) included in the dataset may affect the weight due to
 35 small drifts in instrument performance, modelling errors in PMF, and the prevalence of
 36 transient/variable sources not fully captured by PMF. Therefore, it is important to assess the relative
 37 weight of the two instruments and rebalance if necessary. We define a balanced solution as one in which
 38 there are no systematic differences between quality of fit for different instruments (Slowik et al., 2010;
 39 Crippa et al., 2013a). However, note that variable-to-variable differences in the $e_{i,j}/s_{i,j}$ within the dataset
 40 of a single instrument are permitted (as in standalone PMF).

1 The instrument weighting process follows the method previously proposed by Slowik et al. (2010), in
 2 which weighting is performed by applying a weighting factor C to the uncertainties and evaluated by
 3 comparison of the AMS vs. EESI-TOF residuals. Here we utilise the same weighting method but
 4 propose an improved evaluation metric. Instrument weighting is performed by applying a weighting
 5 factor C to the components of the uncertainty matrix \mathbf{S} corresponding to one of the two instruments.
 6 This increases/decreases the contribution of that instrument's residuals to Q , thereby changing its
 7 weight within the PMF solver. In this paper, we applied the weighting factor, denoted C_{EESI} , to the
 8 columns of \mathbf{S} corresponding to ions measured by the EESI-TOF, according to Eq. (12):

$$9 \quad \begin{cases} (s'_{i,j})_{j=\text{EESI}} = \frac{(s_{i,j})_{j=\text{EESI}}}{C_{\text{EESI}}} \\ (s'_{i,j})_{j=\text{AMS}} = (s_{i,j})_{j=\text{AMS}} \end{cases} \quad (12)$$

10
 11 Note that $C_{\text{EESI}} = 1$ is equivalent to an unweighted solution; and $C_{\text{EESI}} > 1$ means the uncertainty matrix
 12 of EESI-TOF decreases, which upweights the EESI-TOF.

13
 14 As noted above, a balanced solution is defined as one in which the quality of fit to a given ion (assessed
 15 via scaled residuals, e_{ij}/s_{ij}) is independent of the instrument performing the measurement. In previous
 16 work (Slowik et al., 2010; Crippa et al., 2013), the metric used to assess this was the mean of the
 17 absolute scaled residuals. This metric assumes that the optimised solution for each individual instrument
 18 yields approximately the same Q/Q_{exp} . In practice, this may vary between instruments for the reasons
 19 described above. Further, this metric can be unduly influenced by a few large outliers. Therefore, we
 20 employ a new approach which references the residuals from the combined dataset to those obtained
 21 from the final solutions from single-instrument PMF, which having been selected as the optimal
 22 representation of environmental data are assumed to likewise provide the optimised distributions of
 23 single-instrument residuals. The new method is as follows:

24 1) From the result of each single instrument PMF (here AMS PMF, EESI-TOF PMF), calculate
 25 the scaled residual (e_{ij}/s_{ij}) probability distribution over the entire (single instrument) dataset. Here we
 26 denote the scaled residual probability distribution function in the scaled residual (e_{ij}/s_{ij}) space for EESI-
 27 TOF and AMS as $P_{\text{EESI}}(e_{ij}/s_{ij})$ and $P_{\text{AMS}}(e_{ij}/s_{ij})$, respectively.

28 2) Calculate the overlap fraction F_{overlap} between the AMS and EESI-TOF scaled residual
 29 probability distributions from the single instrument solutions, according to Eq. (13):

$$30 \quad F_{\text{overlap}} = \int \min \left(P_{\text{EESI}} \left(\frac{e_{ij}}{s_{ij}} \right), P_{\text{AMS}} \left(\frac{e_{ij}}{s_{ij}} \right) \right) \quad (13)$$

31
 32 where $P_{\text{EESI}}(e_{ij}/s_{ij})$ and $P_{\text{AMS}}(e_{ij}/s_{ij})$ indicates the probability of occurrence of AMS and EESI-TOF at the
 33 point e_{ij}/s_{ij} in scaled residual space, respectively. Given the previously mentioned assumption that the
 34 single-instrument solutions represent the optimal representation of the data for the individual
 35 instruments, the F_{overlap} calculated at this step is the value that should likewise be obtained from a
 36 balanced solution to the combined dataset. Therefore, we define the quantity F_{overlap}^* as the F_{overlap} of
 37 the final single-instrument PMF solutions.

38 3) For the combined dataset, calculate F_{overlap} as a function of a two-dimensional exploration
 39 of the space defined by weighing factor (C_{EESI}) and the number of factors (p). This exploration is
 40 necessary because the scaled residuals have been empirically observed to depend not only on C but also
 41 p (Slowik et al., 2010; Crippa et al., 2013a), likely because p affects the degrees of freedom in the
 42 solution. We select for further analysis the set of solutions in which F_{overlap} does not greatly differ from
 43 F_{overlap}^* , as given by Eq. (14):

1
2
3
4
5
6
7
8
9
10
11
12
13
14
15
16
17
18
19
20
21
22
23
24
25
26
27
28
29
30
31
32
33
34
35
36
37
38
39
40
41
42
43
44
45
46

$$|F_{\text{overlap}}(C, p) - F_{\text{overlap}}^*| < \beta \quad (14)$$

where the threshold of absolute difference is defined as β . Here β is a subjective parameter chosen to allow a manageable number of solutions to be selected for detailed inspection. For computational efficiency, if one or more factors are constrained, we choose $a = 0$ for all constrained factors at this preliminary exploration stage and will explore the a value range(s) for constraint(s) for further bootstrapping analysis once the C and p are determined.

The balanced solutions satisfying Eq. (14) are then evaluated using the same metrics as in standard PMF analysis to select the solution with the greatest explanatory power. This solution is used as the base case for bootstrap analysis and, if one or more factors are constrained, simultaneous randomised a -value trials.

2.3.4 Bootstrap/constraint sensitivity analysis on the combined dataset

Bootstrap analysis (Davison and Hinkley, 1997) is frequently used to characterise solution stability, reproducibility and estimate uncertainties. In typical bootstrap analysis, a set of new input and error matrices are created by random resampling of rows from the original input data and error matrices. The resulting resampled matrices preserve the original dimensions of the input data matrix, but randomly duplicate some time points while excluding others (Paatero et al., 2014). In the present analysis, we combined bootstrap analysis with randomised selection of a values for all constrained factors within predetermined limits defined on a factor-by-factor basis. Since the constrained factors use reference profiles constructed with an estimated AS_k (see Eq. (11)), this combined bootstrap/constraint analysis allows recalculation of AS_k within PMF for any factor with a non-zero a value. As a result, the final reported solution is the average of all accepted bootstrap runs, with uncertainties in factor profiles and time series taken as the standard deviation. To minimise the effect of estimated AS_k on constrained factors, we suggest that in the future this method could be improved by initialisation of constrained factor profiles with randomised AS_k within a predefined range, in conjunction with the existing a -value/bootstrap routine.

Within this analysis, the range of a values explored for a given factor may have a significant effect on the acceptance probability. A very low acceptance probability is undesirable because it is computationally inefficient, while a very high acceptance probability is also undesirable because it implies the solution space is inadequately explored due to excessively restrictive a values (Canonaco et al., 2021). Therefore, we conduct pre-tests to estimate the a value range leading to a reasonable acceptance probability. This is done by a set of 2-dimensional a -value (“multi-2D”) scans in which the a values of two constrained factors are varied stepwise from 0 to 1 with a step size of 0.1 (i.e., 121 runs), while the a values of other constrained factors are held at 0. The results of all multi-2D runs for a given factor are combined to determine the acceptance probability as a function of a value, and upper and lower a value boundaries are assessed. The acceptance criteria are dataset-specific and discussed in the Text S2.4. When the number of constrained factors (p_{ref}) = 2, the multi-2D algorithm is equivalent to an explicit exploration of all possible a value combinations. However, for $p_{ref} > 2$, multi-2D is much more computationally efficient, because it increases as $p_{ref} (p_{ref} - 1)/2$, whereas the explicit method increases as the factorial of p_{ref} . For the datasets used here, in which p_{ref} is 3 (summer) and 4 (winter), the multi-2D approach decreases the number of runs required for a -value pre-scans by factors of ~4 and ~20, respectively.

1 Acceptance criteria consist of both the assessment of specific features of selected factor profiles/time
2 series (see Text S2.4), as well as a general evaluation of whether the solution is qualitatively similar to
3 the base case. That is, we require that the time series of each factor from a PMF run to be unambiguously
4 related to the corresponding base case factor (Stefenelli et al., 2019; Vlachou et al., 2019; Tong et al.,
5 2021). The key steps of this method are summarised below: 1) identify a base case, which as discussed
6 above is defined by a weighting factor C , number of factors p , and set of constrained factors with the a
7 value set to 0; 2) calculate the Spearman correlation between the time series of base case and the multi-
8 2D scans, which yields a correlation matrix with the highest correlation values on the diagonal; 3) each
9 correlation coefficient on the matrix diagonal must be by a statistically significant margin (using
10 different confidence levels from a t test) than any value on the intersecting row or column. In the current
11 study, we selected a confidence level of 0 for this base case/bootstrap correlation test, representing the
12 most permissive application of this criterion. That is, we require only that the diagonal matrix mentioned
13 above can be constructed, i.e., that there is a unique 1:1 correspondence between base case factors and
14 factors from the bootstrap/ a -value analysis.

15
16 The final set of PMF runs consisted of 1000 bootstrap runs, conducted at a single combination of C_{EESI}
17 and p , with a values randomly selected with a step size of 0.05 for summer and 0.1 for winter within
18 the factor-specific limits determined via the multi-2D pre-scans. The same acceptance criteria utilised
19 for the multi-2D pre-scans were also used for the bootstrap runs. As a final solution, we report the mean
20 factor profiles and time series determined from all accepted bootstrap runs, with the standard deviation
21 taken to represent the uncertainty of the analysis procedure. Although not currently implemented within
22 the analysis software used, we note that in theory it would be possible to additionally include random
23 C_{EESI} selection (within a predefined range corresponding to balanced solutions) and randomised AS_k for
24 constrained profiles (within a user-defined range) in this stage of the analysis and in calculation of the
25 final model outputs.

26 27 28 **3. Results**

29
30 We have conducted cPMF analysis on datasets collected from the summer and winter campaigns. The
31 parameters for the PMF analysis of the combined dataset and the re-analysed summer and winter
32 datasets are summarised in Table 1. We re-ran the conventional PMF on the summer and the winter
33 data, obtaining results similar to Stefenelli et al. (2019) and Qi et al. (2019), as discussed in Text S2
34 in the Supplement. Other technical details of method validation and solution selections are also explained
35 in the Supplement (from the Text S2.2 to Text S2.4), including reference profile construction, the
36 determination of C_{EESI} and number of factors p , and the determination of case-specific a value range
37 and acceptance criteria for bootstrap analysis. Table 2 summarises these case-specific facts for summer
38 and winter datasets, including a value range for constrained factors, criteria for a value range and
39 accepted bootstrap run selection, and the number of accepted runs from the final combined bootstrap.

40
41 Here we present final results from the cPMF analysis of the summer and winter campaigns in Sect 3.1.1
42 and Sect 3.1.2, respectively. The final solutions are reported as the average of all accepted bootstrap/ a -
43 value randomisation runs (764 for summer, 308 for winter), with uncertainties corresponding to the
44 standard deviation. As the NO^+ and NO_2^+ signals are included in these two datasets and they can result
45 from either organic or inorganic nitrate, we estimate the organic and inorganic contributions to the NO^+
46 and NO_2^+ signal in each factor using the method of Kiendler-Scharr et al. (2016) (see Text S3). We
47 compare the cPMF factors to their counterparts from the standalone AMS and EESI-TOF solutions, for

1 cases where a clear factor-to-factor correspondence exists. The further exploration on EESI-TOF
 2 sensitivities to resolved factors are discussed in Sect 3.2.

3

4 Due to the complexity of the analysed datasets (2 seasons \times 3 PMF methods), we use the following
 5 convention for identifying factors: factorName_{season,method}, where “factorName” is the name of the factor
 6 (e.g., COA for cooking-related organic aerosol), “season” denotes either the summer (“S”) or winter
 7 (“W”) dataset, and “method” refers to PMF on standalone AMS dataset (“A”), standalone EESI-TOF
 8 dataset (“E”), or combined dataset (“C”). For example, COA_{S,C} stands for the cooking-related factor
 9 retrieved from cPMF applied to the summer dataset.

10

11 **Table. 1** Summary of parameters for the PMF analysis of re-analysed summer and winter datasets, and
 12 the combined dataset. There are 257 ions that are found in PMF input matrices for both the summer and
 13 winter datasets (common ions are listed in the Table S1). All datasets include AMS measurements of
 14 NO⁺ and NO₂⁺.

		EESI-TOF	AMS	Combined
Summer	Matrix dimensions (time points \times m/z)	1779 \times 507	1779 \times 287	1779 \times 794
	Time period	20 to 26 June 2016	20 to 26 June 2016	20 to 26 June 2016
	Time resolution (min)	5	5	5
	Range of p analysed	6	6	5-10
Winter	Matrix dimensions (time points \times m/z)	6142 \times 892	6142 \times 258	6142 \times 1150
	Time period	25 Jan to 4 Feb 2017	25 Jan to 4 Feb 2017	25 Jan to 4 Feb 2017
	Time resolution (min)	1	1	1
	Range of p analysed	12	8	7-14

15

16 **Table. 2** Summary of a value range for constrained factors, criteria for a value range and accepted
 17 bootstrap run selection and the number of accepted runs from the final combined bootstrap/ a -value
 18 analysis for the summer and winter datasets.

19

Dataset	Constrained factor	a value range	Criteria	Accepted runs
Zurich summer	HOA _{S,C}	$0 \leq a \leq 0.2$	1). COA _{S,C} : $\frac{C_3H_3O^+}{C_3H_5O^+} \geq 5$ 2). InorgNits _{S,C} : $\frac{CO_2^+}{NO^+ + NO_2^+} \leq 0.035$ 3). Base case vs. Bootstrap correlation test at confidence level = 0	764 (76.4 %)
	COA _{S,C}	$0 \leq a \leq 0.2$		
	Inorganic nitrate (InorgNits _{S,C})	$0 \leq a \leq 0.5$		
Zurich winter	HOA _{W,C}	$0 \leq a \leq 0.9$	1). CSOA _{W,C} : $f_{mass}(\text{nicotine}) \geq 0.96$ 2). C ₂ H ₄ O ₂ ⁺ intensity: LABB _{W,C} – MABB _{W,C} > 0 3). C ₆ H ₁₀ O ₅ intensity: LABB _{W,C} – MABB _{W,C} > 0 4). Base case vs. Bootstrap correlation test at confidence level = 0	308 (30.8 %)
	COA _{W,C}	$0 \leq a \leq 0.3$		
	Inorganic nitrate (InorgNit _{W,C})	$0 \leq a \leq 0.5$		

	CSOA _{w,c}	$0 \leq a \leq 0.6$	
--	---------------------	---------------------	--

1

2

3.1 cPMF results

3

4

5

3.1.1 cPMF analysis: Zurich summer

6 Eight factors were resolved from the Zurich summer campaign: HOA_{s,c}, COA_{s,c}, CSOA_{s,c}, InorgNits_{s,c},
7 two daytime SOA factors (DaySOA1_{s,c} and DaySOA2_{s,c}), and two nighttime SOA factors
8 (NightSOA1_{s,c} and NightSOA2_{s,c}). The mean time series, diurnal cycles, and the mass spectra of these
9 factors over 764 accepted runs are shown in Fig. 3, together with the time series from AMS-only PMF
10 and/or EESI-TOF-only PMF when the corresponding standalone factor(s) exist. An estimate of
11 campaign-average percent uncertainty in the mass concentration of each factor, calculated as the median
12 of the standard deviation across all accepted runs, is given in Table S2. Many factor characteristics from
13 cPMF resemble those previously discussed in detail for single-instrument AMS PMF and/or EESI-TOF
14 PMF (Stefenelli et al., 2019). Therefore, only a summary discussion of these characteristics is presented
15 here, and we focus on new information and/or differences obtained by the cPMF analysis. Recall that
16 factor profiles for HOA_{s,c}, COA_{s,c}, and InorgNits_{s,c} are constrained as discussed above.

17

18 **HOA_{s,c}** --- The AMS mass spectrum is dominated by the C_nH_{2n+1}⁺, and C_nH_{2n-1}⁺ series, consistent with
19 *n*-alkanes and branched alkanes (Zhang et al., 2005; Lanz et al., 2007; Ulbrich et al., 2009; Ng et al.,
20 2011a; Qi et al., 2019; Stefenelli et al., 2019). The diurnal cycle of HOA_{s,c} has three clear peaks (see
21 Fig. 3b), however, compared to HOA_{s,A} from Stefenelli et al. (2019), their intensities are weaker.
22 Specifically, the morning peak intensity ratio to the evening peak intensity is almost 1 in the HOA_{s,A}
23 factor, whereas in HOA_{s,c}, the morning peak is ~1/3 of the evening peak. In terms of contribution to
24 total OA, the HOA_{s,A} factor contributes 5.8 % (0.177 μg m⁻³) of the total OA, whereas in the cPMF
25 analysis, this factor only contributes 3.1 % (0.092 μg m⁻³) of the total OA.

26

27 **COA_{s,c}** --- This factor is characterised by long-chain fatty acids and alcohols, e.g., coronaric acid and/or
28 its isomers at *m/z* 319.2 ([C₁₈H₃₂O₃]Na⁺), oleic acid and/or its isomers at *m/z* 305.2 ([C₁₈H₃₄O₂]Na⁺),
29 and 2-oxo-tetradecanoic acid and/or its isomers at *m/z* 293.2 ([C₁₆H₃₀O₃]Na⁺). Similar to previous work,
30 the AMS profile shows both alkyl fragments and slightly oxygenated ions, consistent with aliphatic
31 acids from cooking oils (Hu et al., 2016). The AMS profile is characterised by a high ratio of C₃H₃O⁺
32 to C₃H₅O⁺ (~5 here), slightly higher than in other studies (Sun et al., 2016a; Sun et al., 2016b; Xu et al.,
33 2019; Zhao et al., 2019), as well as high contributions from C₅H₈O⁺, C₆H₁₀O⁺ and C₇H₁₂O⁺. Both cPMF
34 and single instrument PMF analyses yield peaks during lunch (~11:30 to 13:30) and dinner (~18:30 to
35 20:30). The time series of COA_{s,c} is strongly correlated with those of the single instrument solutions,
36 with Pearson's *r*² of 0.846 and 0.634 against COA_{s,A} and COA_{s,E}, respectively.

37

38 **CSOA_{s,c}** --- The EESI-TOF factor profile is dominated by nicotine (detected as [C₁₀H₁₃N₂]H⁺) at *m/z*
39 163.12 and levoglucosan at *m/z* 185.042 ([C₆H₁₀O₅]Na⁺), which derives from pyrolysis of the cellulose
40 present in tobacco (Talhout et al., 2006). In the AMS profile, this factor accounts for 79.3 % of the
41 signal from C₅H₁₀N⁺ at *m/z* 84.081, which is attributed to a fragment of *n*-methyl pyrrolidine and
42 previously identified as a tracer for cigarette smoke (Struckmeier et al., 2016). The time series of
43 CSOA_{s,c} correlates with that of the AMS-only and EESI-TOF solutions, with *r*² of 0.922 and 0.965,
44 respectively. The diurnal cycles from the combined and single-instrument solutions are likewise
45 correlated, showing high concentrations at night and low concentration during daytime.

1
2 **InorgNits_{S,C}** --- Among the accepted bootstrap runs, the mean $\text{CO}_2^+ / (\text{NO}^+ + \text{NO}_2^+)$ ratio is 0.0346, slightly
3 higher than the ratio of 0.0345 observed during the NH_4NO_3 calibration period, probably due to 1)
4 uncertainties in the constrained profile, and/or 2) a small amount of OA apportioned to this factor. The
5 time series of this factor correlates with AMS nitrate (NO_3^-), NO^+ and NO_2^+ time series, with r^2 of 0.654,
6 0.645 and 0.956, respectively. Regarding the mass fraction, approximately 48.5 % of the NO^+ signal
7 and 78.0 % of the NO_2^+ signal are apportioned to this factor, followed by the two $\text{NightSOA}_{S,C}$ factors.
8 This is consistent with the overall NO^+ and NO_2^+ signals deriving not only from inorganic nitrate, but
9 also from organonitrates (in other factors).

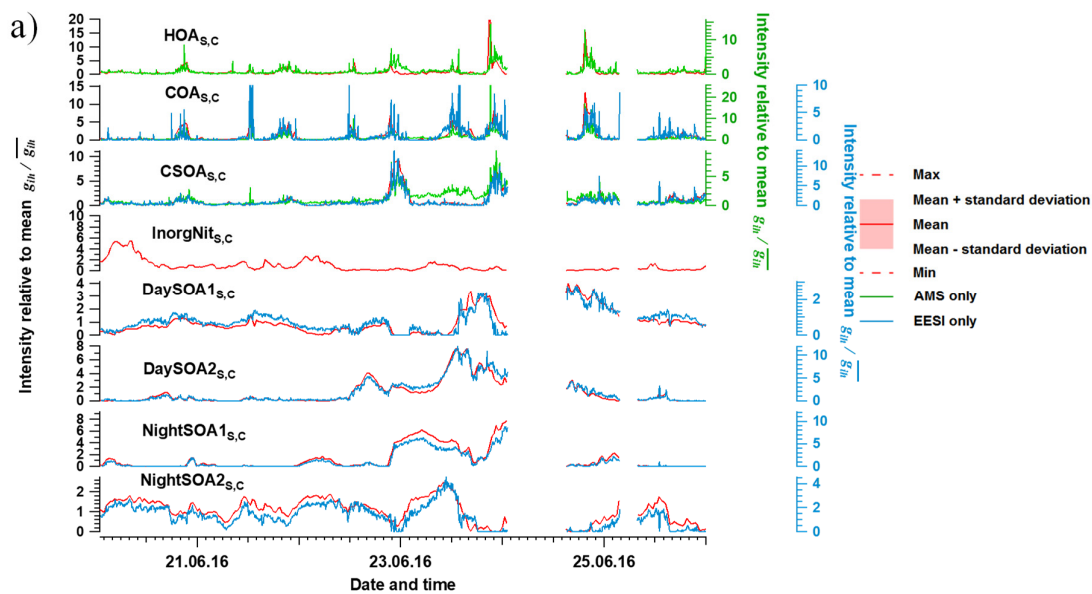
10

11 **DaySOA1_{S,C} and DaySOA2_{S,C}** --- The cPMF analysis yields two SOA factors elevated during daytime,
12 denoted DaySOA1_{S,C} and DaySOA2_{S,C}. The EESI-TOF spectra are similar to two factors retrieved from
13 EESI-TOF-only PMF analysis by Stefenelli et al. (2019), but were not resolved in AMS-only PMF,
14 where only more- and less-oxygenated SOA factors ($\text{MO-OOA}_{S,A}$ and $\text{LO-OOA}_{S,A}$) were obtained.
15 These factors contain strong signatures from terpene oxidation products, e.g., monoterpene-derived ions
16 ($\text{C}_{10}\text{H}_{16}\text{O}_x$, $x=5, 6, 7$) and sesquiterpene oxidation products ($\text{C}_{15}\text{H}_{24}\text{O}_x$, $x=3, 4, 5$). A detailed comparison
17 of the two DaySOA factors from the cPMF analysis to the $\text{LO-OOA}_{S,A}$ and $\text{MO-OOA}_{S,A}$ factors from
18 AMS-only PMF is shown in Fig. S31, and a comparison between the two $\text{DaySOA}_{S,C}$ factors and
19 $\text{DaySOA}_{S,E}$ factors are shown in Figs. S32 a) and b), respectively. The AMS ions in these two factors
20 are characterised by a strong CO_2^+ signal, similar to the $\text{LO-OOA}_{S,A}$ and $\text{MO-OOA}_{S,A}$ factors, indicating
21 they largely consist of oxygenated OA, consistent with the EESI-TOF spectra. We calculate frac_{ON}
22 for DaySOA1_{S,C} and DaySOA2_{S,C} to be 0.869 and 1.000, respectively, demonstrating that the NO^+ and
23 NO_2^+ signal in these factors is dominated by organonitrates. Regarding the time series, DaySOA1_{S,C} and
24 DaySOA2_{S,C} correlate strongly with DaySOA1_{S,E} and DaySOA2_{S,E}, with r^2 of 0.883 and 0.977,
25 respectively. The diurnal patterns of DaySOA1_{S,C} and DaySOA2_{S,C} are consistent with the diurnal
26 patterns of DaySOA1_{S,E} and DaySOA2_{S,E}. The diurnal patterns of both factors show an enhancement in
27 the afternoon and the evening, which distinguish these SOAs from other SOAs: DaySOA1_{S,C} exhibits
28 almost a factor of 2 enhancement in signal between 15:00 and 21:00 compared to the morning, whereas
29 the DaySOA2_{S,C} exhibits the same magnitude of enhancement in signal around 12:00 to 17:00.

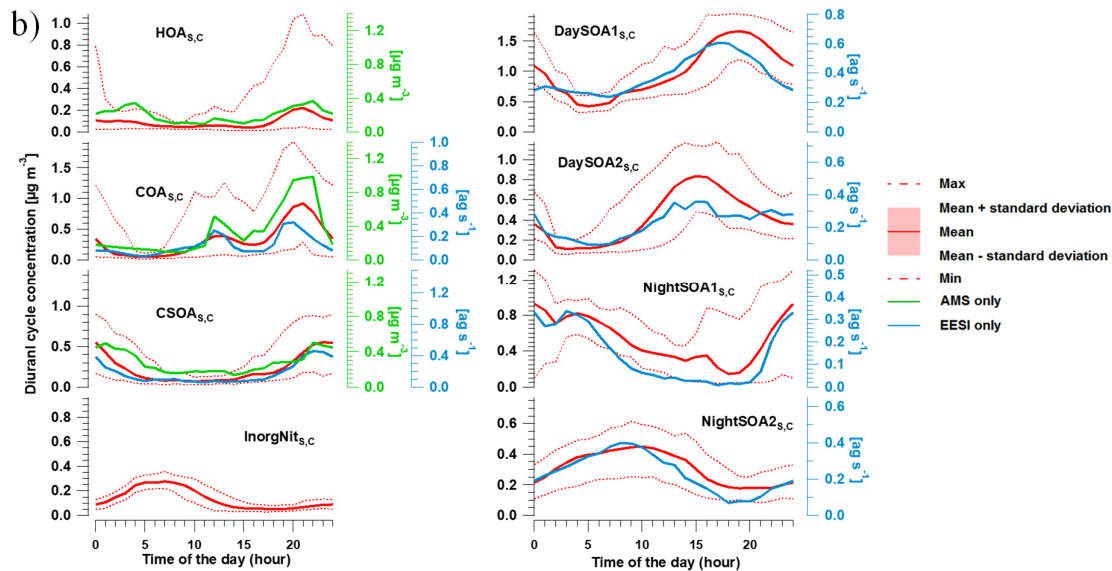
30

31 **NightSOA1_{S,C} and NightSOA2_{S,C}** --- We retrieve two SOA factors that are enhanced overnight and in
32 the early morning, denoted NightSOA1_{S,C} and NightSOA2_{S,C}. Their factor profiles and time
33 series/diurnals closely resemble those of NightSOA1_{S,E} and NightSOA2_{S,E} (see Figs. S32c and S32d).
34 Similar to the $\text{DaySOA}_{S,C}$ factors, terpene oxidation products are evident. However, the composition is
35 weighted towards less oxygenated and more volatile terpene oxidation products, e.g., $\text{C}_{10}\text{H}_{16}\text{O}_2$ and
36 $\text{C}_{10}\text{H}_{16}\text{O}_3$, which likely partition to the particle phase at night when temperature decreases. In addition,
37 signals consistent with monoterpene-derived organonitrates are also evident, e.g., the $\text{C}_{10}\text{H}_{17}\text{O}_{6-8}\text{N}$ and
38 $\text{C}_{10}\text{H}_{15}\text{O}_{6-9}\text{N}$ series, which are consistent with night time oxidation of monoterpenes by NO_3 radicals
39 (Xu et al., 2015; Faxon et al., 2018; Zhang et al., 2018). The AMS ions in these two factors are
40 characterised by a strong CO_2^+ signal and also a relatively high NO^+ signal compared to $\Sigma\text{DaySOA}_{S,C}$.
41 The ratio of $\text{NO}^+ / \text{NO}_2^+$ is 4.55 and 8.24 for NightSOA1_{S,C} and NightSOA2_{S,C}, respectively, yielding
42 frac_{ON} for NightSOA1_{S,C} and NightSOA2_{S,C} of 0.798 and 1, indicating high organonitrate content.
43 These two factors correlate well with $\Sigma\text{NightSOA}_{S,E}$, reaching r^2 of 0.975 and 0.897, following in
44 general the same diurnal patterns, with NightSOA1_{S,C} peaking from 22:00 to 05:00 and NightSOA1_{S,C}
45 peaking from 04:00 to 12:00.

1



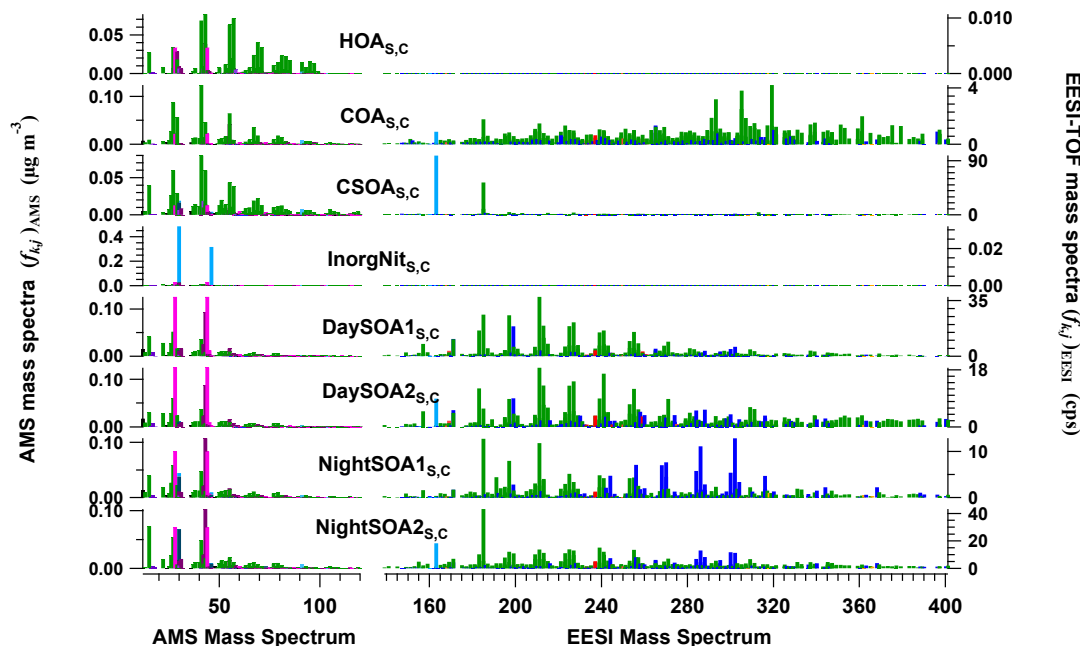
2



3

C) AMS ions: C_xH_y , C_xH_yO , $C_xH_yO_{z>1}$ (incl. CO^+ and CO_2^+)
 C_xH_yN , $C_xH_yON_z$,
 NO_x from inorganic nitrate, NO_x from organic nitrate

EESI ions: $C_xH_yO_z$, $C_xH_yO_zN_p$, $C_xH_yN_p$, $C_xH_yO_zS_j$



1
2 Figure 3. Mean factor time series (a), diurnal cycles (b) and factor profiles (c) from the 764 accepted
3 bootstrap runs from cPMF analysis. In a), the average factor time series are shown in red, and
4 corresponding AMS and/or EESI-TOF factors from standalone PMF are shown in green and blue,
5 respectively. Shaded areas represent the standard deviation across all accepted runs and are summarised
6 in Table S2. In b), the average diurnal cycles are displayed as red solid lines. Shaded areas denote the
7 standard deviation over the average diurnal from individual solutions over all 764 accepted runs.
8 Dashed lines denote the maximum and minimum mean diurnal observed within these 764 runs. For
9 comparison, the AMS and EESI-TOF PMF factor time series and diurnal cycles from the individual
10 dataset in Stefenelli et al. (2019) are shown in green and blue respectively for related factors. In c), the
11 average factor profiles are coloured by different ion families. Here, the AMS factor profiles are in the
12 unit of $\mu\text{g m}^{-3}$ (each factor sums to $1 \mu\text{g m}^{-3}$), whereas the EESI-TOF spectra are in the unit of cps (each
13 factor sums to the total signal derived from $1 \mu\text{g m}^{-3}$ of the factor). Note that the NO^+ and NO_2^+
14 signal is divided into inorganic and organic contributions.

16 3.1.2 cPMF analysis: Zurich winter

17
18 Twelve factors were resolved from cPMF analysis of the Zurich winter campaign: $HOA_{w,C}$, $COA_{w,C}$,
19 $InorgNit_{w,C}$, $CSOA_{w,C}$, $SOA1_{w,C}$, $SOA2_{w,C}$, a more-aged biomass burning OA ($MABB_{w,C}$), two less-
20 aged biomass burning OAs ($LABB1_{w,C}$ and $LABB2_{w,C}$), two nitrogen-containing OA factors
21 ($NitOA1_{w,C}$ and $NitOA2_{w,C}$), and a factor related to a specific local event ($EVENT_{w,C}$). Because no
22 significant chemical differences are apparent between $LABB1_{w,C}$ and $LABB2_{w,C}$ (see Figs. S33 and
23 S34), they are aggregated to a single $LABB_{w,C}$ factor for presentation. Therefore, there are 11 factors
24 presented below. The average time series and mass spectra of these factors among 308 accepted runs
25 are shown in Fig. 4. The factor profiles for $HOA_{w,C}$, $COA_{w,C}$, $InorgNit_{w,C}$, and $CSOA_{w,C}$ are constrained
26 as described previously. Similar to the summer dataset, uncertainties in the factor mass concentrations
27 are summarised in Table S2.

28

1 **HOA_{w,c}** --- This factor is dominated by the C_nH_{2n+1}⁺, and C_nH_{2n-1}⁺ series, consistent with *n*-alkanes and
2 branched alkanes, with lower CO⁺ and CO₂⁺ content than the HOA_{s,c}. The HOA_{w,c} time series
3 correlates strongly with HOA_{w,A} (*r*² of 0.913).

4 **COA_{w,c}** --- The COA_{w,c} profile is characterised by long-chain fatty acids and alcohols e.g., coronaric
5 acid and/or its isomers at *m/z* 319.2 ([C₁₈H₃₂O₃]Na⁺), oleic acid and/or its isomers at *m/z* 305.2
6 ([C₁₈H₃₄O₂]Na⁺), and 2-oxo-tetradecanoic acid and/or its isomers at *m/z* 293.2 ([C₁₆H₃₀O₃]Na⁺), and in
7 the AMS, a combination of alkyl fragments and slightly oxygenated ions from aliphatic acids from
8 cooking oils, including C₃H₈O⁺, C₆H₁₀O⁺ and C₇H₁₂O⁺. These are key features of the constrained
9 reference profile (0 ≤ *a* ≤ 0.3) (Qi et al., 2019) and COA factors found in other studies (Stefenelli et al.,
10 2019; Tong et al., 2021). The COA_{w,c} time series correlates with the corresponding single instrument
11 analyses, exhibiting *r*² of 0.894, and 0.798, with COA_{w,A} and COA_{w,E}, respectively.

12 **InorgNit_{w,c}** --- As noted in Text S2.2, the NO⁺/NO₂⁺ ratio of this factor (2.42) is higher than that of
13 pure NH₄NO₃ measured onsite (1.58), consistent with the presence of other inorganic nitrate sources
14 such as KNO₃. Also, the mean CO₂⁺/(NO⁺+NO₂⁺) ratio is 0.0371, higher than the ratio of 0.0261 from
15 the constructed InorgNit_{w,c} profile, probably due to 1) uncertainties in the constrained profile, and/or
16 2) a small amount of OA apportioned to this factor. The time series of this factor shows high correlations
17 with the AMS nitrate (NO₃⁻), NO⁺ and NO₂⁺ time series, with *r*² of 0.739, 0.792 and 0.754, respectively.
18 Regarding the mass fraction, only 13.7% of the NO⁺ signal and 13.2 % of the NO₂⁺ signal are
19 apportioned to this factor. The considerable fractions of the NO⁺ and NO₂⁺ signal from inorganic nitrate
20 and organonitrates in other factors are estimated as discussed above (Kiendler-Scharr et al., 2016) and
21 will be interpreted later for the relevant factors (as summarised in Table S1).
22

23 **CSOA_{w,c}** --- Similar to CSOA_{s,c}, nicotine at *m/z* 163.12 and levoglucosan at *m/z* 185.042 were found
24 to be the two highest peaks in the EESI-TOF mass spectra, contributing 8.75 % and 4.56 % of the EESI-
25 TOF signal. The time series of this factor resolved from cPMF analysis correlates with CSOA_{w,E} (*r*² =
26 0.662). Similar to CSOA_{w,c}, the fragment of cigarette smoke tracer *n*-methyl pyrrolidine C₅H₁₀N⁺ at
27 *m/z* 84.081 is also found here. This is a minor factor, comprising 2.4 % of OA.
28

29 **SOA1_{w,c} and SOA2_{w,c}** --- these two factors have different temporal patterns. SOA1_{w,c} decreased
30 gradually from 26 to 30 January, whereas SOA2_{w,c} increased from 26 January and fluctuated at high
31 level from 28 to 31 January and then decreased from 1 February on. From the AMS perspective, both
32 factors are characterised by high NO⁺, NO₂⁺ and CO₂⁺ signal compared to other organic ions.
33 Organonitrates account for all NO⁺ and NO₂⁺ signals in SOA1_{w,c}, but contribute nothing in SOA2_{w,c}.
34 Aside from the NO⁺ and NO₂⁺ ions, these AMS spectra are similar to the profiles of MO-OOA_{w,A} and
35 LO-OOA_{w,A} which are characterised by high CO₂⁺ signal. Major ions in the EESI-TOF profile include
36 C₁₀H₁₆O_x (*x* = 3, 4, 5), C₉H₁₄O_x (*x* = 3, 4), C₈H₁₂O_x (*x* = 4, 5), C₁₀H₁₈O₄, and C₁₀H₁₄O₅, which are also
37 found in secondary biomass burning (three MABB_{w,E} factors) and/or terpene oxidation factors
38 (SOA1_{w,E} and SOA2_{w,E}) from Qi et al. (2019). However, the H:C ratio of these two factors from the
39 EESI-TOF component (1.578 and 1.588 for SOA1_{w,c} and SOA2_{w,c}, respectively) is less than that of
40 DaySOA1_{s,c} (1.650) and DaySOA2_{s,c} (1.672), suggesting an increased contribution from aromatic
41 precursors.
42

43 **Biomass burning factors (LABB_{w,c} and MABB_{w,c})** --- We resolve a less-aged biomass burning
44 factor (LABB_{w,c}, which, as mentioned above, is the aggregate of two similar LABB factors), and a
45 more-aged biomass burning factor (MABB_{w,c}). Consistent with Qi et al. (2019), the EESI-TOF
46 component of LABB_{w,c} is characterised by a large signal from [C₆H₁₀O₅]Na⁺ (mainly levoglucosan)

1 (20.4 %), and MABB_{w,c} by a smaller but notably non-zero one (6.21 %). In addition, 76.7 % and 11.9 %
2 of the total levoglucosan signal is apportioned to LABB_{w,c}, and MABB_{w,c}, respectively. The difference
3 in the fraction of total levoglucosan apportioned to these two factors suggests different degrees of ageing
4 of biomass burning-emitted OA. The AMS spectrum of the BBOA_{w,A} factor is characterised by
5 C₂H₄O₂⁺ and C₃H₅O₂⁺, which are typical fragments of anhydrosugars, such as levoglucosan (Alfarra et
6 al., 2007; Lanz et al., 2007; Sun et al., 2011). These ions are also present in LABB_{w,c} and MABB_{w,c}
7 and are higher in LABB_{w,c} (1.91 % vs 0.879 % for C₂H₄O₂⁺ and 0.978 % vs 0.323 % for C₃H₅O₂⁺). In
8 addition, the ratio of C₂H₄O₂⁺ to CO₂⁺ is 0.396 and 0.092 for LABB_{w,c} and MABB_{w,c}, respectively,
9 supporting the separation of these factors based on different degrees of ageing.

10

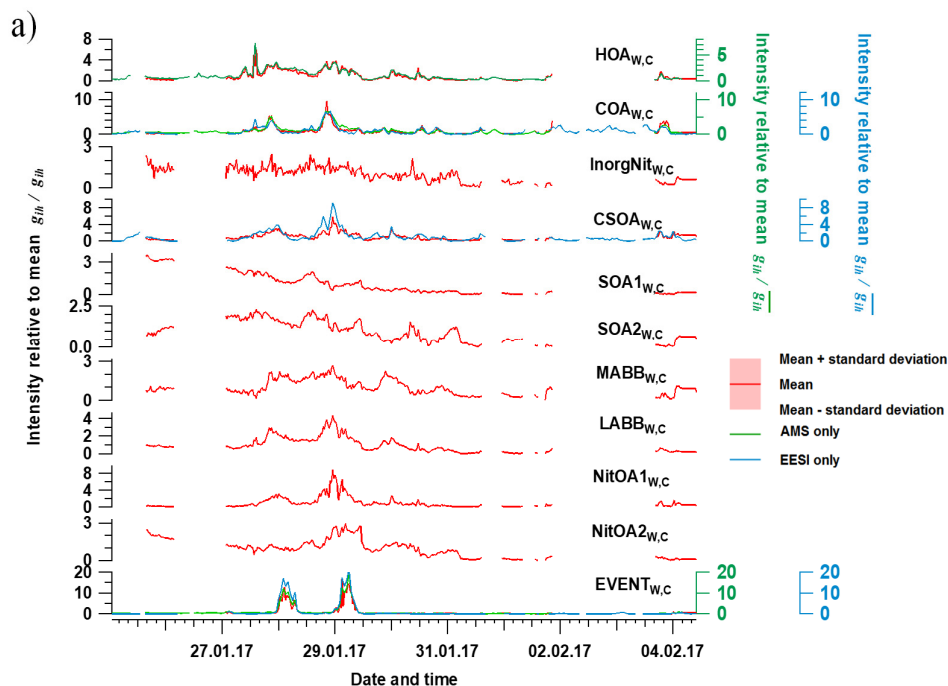
11 **EVENT_{w,c}** --- This factor is low throughout the campaign except for the nights of 28 and 29 January
12 from 00.00 to 07.00 UTC+2, where large peaks are observed. Therefore, it likely corresponds to a
13 specific event near the sampling location. The mass spectrum features ions at *m/z* 174.08, 185.04 and
14 195.06, tentatively assigned to [C₈H₁₁N₂O]Na⁺, [C₆H₁₀O₅]Na⁺ and [C₈H₁₂O₄]Na⁺ from the EESI-TOF
15 part and at *m/z* 15.024 (CH₃⁺), 27.027 (C₂H₃⁺), 31.018 (CH₃O⁺), and 43.018 (C₂H₃O⁺) from the AMS
16 part. Qi et al. (2019) observed a very similar factor in standalone EESI-TOF PMF, which was tentatively
17 attributed to the Zurich gaming festival and/or plastic burning in a nearby restaurant. The factor includes
18 large contributions from C₈H₁₂O₄, which likely represents 1,2-cyclohexane dicarboxylic acid diisononyl
19 ester, a plasticiser for the manufacture of food packaging. In the AMS spectrum, large signals from NO⁺
20 (7.36%) and NO₂⁺ (2.03 %) are also observed, with 46.6 % of the NO⁺ signal and 23.6% of the NO₂⁺
21 signal assigned to organonitrates. Similar to Qi et al. (2019), the AMS spectrum is also dominated by
22 the ions in the C_xH_yO_z⁺ group.

23

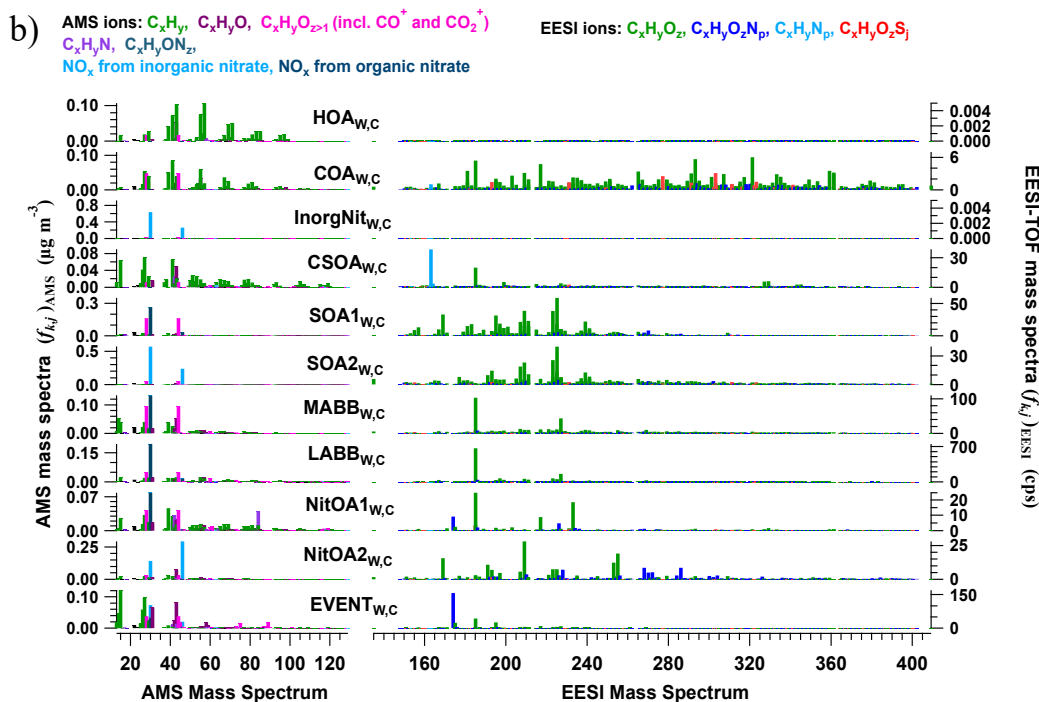
24 **NitOA1_{w,c}**--- this factor is characterised by a high signal of C₅H₁₀N⁺ at *m/z* 84.081, contributing 4.02 %
25 to the AMS intensity in this factor (no other factor exceeds 0.16 %) while 97.0 % of the C₅H₁₀N⁺ mass
26 is apportioned to this factor. This ion is considered to be a tracer of cigarette smoking (Struckmeier et
27 al., 2016), however, different from typical CSOA mass spectra, this factor also has high signal from
28 CO₂⁺, suggesting a contribution from secondary formation processes. Similar to other OA factors, this
29 factor also has a considerable fraction of NO⁺ and NO₂⁺ signal, attributed entirely to organonitrates. For
30 the EESI-TOF component, this factor is characterised by [C₈H₁₁N₂O]Na⁺, levoglucosan and
31 [C₈H₁₁N₂O]Na⁺, [C₆H₁₀O₅]Na⁺ and [C₉H₁₂O₄]Na⁺ and [C₁₁H₁₄O₄]Na⁺, suggesting this factor may also
32 be influenced by fresh biomass burning.

33

34 **NitOA2_{w,c}** --- this factor is characterised by a high fraction of total signal from the CHON group in the
35 EESI-TOF analysis (38.5 %). Among these ions, [C₇H₁₁O₆N]Na⁺ at *m/z* 228.048, [C₁₀H₁₅O₆N]Na⁺ at
36 *m/z* 268.079, and [C₁₀H₁₇O₇N]Na⁺ at *m/z* 286.090 are the three highest ions, contributing 1.65 %, 1.99 %,
37 and 1.98 %, respectively. There are also some typical ions with high intensity from biomass burning
38 ageing (Qi et al., 2019; Stefenelli et al., 2019), e.g., [C₉H₁₄O₄]Na⁺ at *m/z* 209.078, [C₁₀H₁₄O₆]Na⁺ at *m/z*
39 253.068, and [C₁₀H₁₆O₆]Na⁺ at *m/z* 255.084, contributing 6.47 %, 2.85 %, and 4.39 %, respectively.
40 This may suggest a contribution from biomass burning activities. From the AMS perspective, this factor
41 is characterised by high NO⁺ and NO₂⁺ signal, in which all of the NO⁺ and NO₂⁺ signals are produced
42 from inorganic nitrates (see Table S1), with the other ions being qualitatively similar to OOA-type
43 spectra.



1



2

3 Figure 4. Average factor time series (a) and factor profiles (b), which are calculated as the mean of all
 4 accepted bootstrap runs (308 runs in total). In a), the average factor time series are shown in red, and
 5 corresponding AMS and/or EESI-TOF factors from standalone PMF are shown in green and blue,
 6 respectively. Shaded areas represent the standard deviation across all accepted runs and are summarised
 7 in Table S2. In b), the average factor profiles are coloured by different ion families. Here, the AMS
 8 factor profiles are in the unit of $\mu\text{g m}^{-3}$ (each factor sums to $1 \mu\text{g m}^{-3}$), whereas the EESI-TOF spectra
 9 are in the unit of cps (each factor sums to total signal derived from $1 \mu\text{g m}^{-3}$ of the factor). Note that the
 10 NO^+ and NO_2^+ signal is divided into inorganic and organic contributions.

1
2
3
4
5
6
7
8
9
10
11
12
13
14
15
16
17
18
19
20
21
22
23
24
25
26
27
28
29
30
31
32
33
34
35
36
37
38
39
40
41
42
43
44
45
46
47

3.2 EESI-TOF sensitivity to resolved factors

AMS and EESI-TOF contributions to the factor profiles are intrinsically linked by cPMF. That is, for each individual factor the two instrument profiles by definition describe the same OA fraction. Therefore, the EESI-TOF sensitivity to a factor AS_k can be calculated according to Eq. (10). Note that this calculation depends on the assumptions that (1) both instruments are well-represented in the solution; (2) the PMF solution is of high quality (i.e., factors are all meaningful and well-separated, without significant mixing or splitting); (3) solution uncertainties are not so high as to preclude quantitative interpretation of the results. Assumption (1) was discussed earlier in the context of instrument weighting, and assumption (2) is supported by the interpretability of the factors as presented in the previous section. By performing the cPMF analysis on a large number of runs combining bootstrap analysis and a -value exploration, we can estimate uncertainties in the calculated sensitivities imposed by the analysis model, as presented below, thereby addressing assumptions (2) and (3).

The datasets analysed here were taken from the first field deployments of the EESI-TOF. As a result, operational protocols were not yet fully standardised across campaigns. Specifically, we lack reliable on-site calibration with a chemical standard common to the two campaigns (this was attempted but the measurements were evaluated to be unreliable during post-analysis due to operational problems). Therefore, to enable comparison of relative factor sensitivities between the summer and winter campaigns, we select COA as a reference. That is, we assume $AS_{COA} = AS_{COA_{S,C}} = AS_{COA_{W,C}}$. We choose COA because it is the only factor that both (1) appears in all four single-instrument datasets (i.e., summer and winter, AMS and EESI-TOF) and (2) compared to other factors, is less likely to significantly change in composition between the campaigns (in contrast to, e.g., SOA in Zurich, which is known to have significantly different precursors in summer and winter). Therefore, all sensitivities below are reported as $(AS_k / \overline{AS_{COA}})$, in which AS_k is calculated in every bootstrap run, and then referenced to $\overline{AS_{COA}}$ (the mean AS_{COA} calculated over all bootstrap runs). Here k denotes a given factor from the (summer or winter) cPMF solutions. Note that EESI-TOF sensitivities to HOA and InorgNit are not discussed here, since they are undetectable by the EESI-TOF (as configured for these campaigns; see Sect.2.2.2) and therefore constrained to be ~ 0.01 cps / ($\mu\text{g m}^{-3}$). The mean and standard deviation of factor-dependent $AS_k / \overline{AS_{COA}}$ for the summer and winter datasets are shown in Fig. 5, with histograms summarising all accepted runs shown in Fig. S35 and Fig. S36.

For ease of viewing, the factors in Fig. 5 are collected into related groups. We also calculate the AS_k 's for several factor aggregations. First, five factors that are likely related to biomass burning ($\text{LABB}_{W,C}$, $\text{MABB}_{W,C}$, $\text{NitOA1}_{W,C}$, $\text{NitOA2}_{W,C}$ and $\text{EVENT}_{W,C}$), are denoted as the “ ΣBB ” factor. Additionally, we separately aggregate the two $\text{DaySOA}_{S,C}$ and two $\text{NightSOA}_{S,C}$ factors, denoted “ $\Sigma\text{DaySOA}_{S,C}$ ” and “ $\Sigma\text{NightSOA}_{S,C}$ ”, respectively. As seen in Fig. 5 (as well as in Figs. S35 and S36 and Table S3), the relative uncertainty from the summer factors is systematically lower than for the winter factors within the accepted solutions. This may indicate higher source apportionment quality and solution stability for the former but is also related to the sub-division of factors related to primary biomass burning-related factors, as discussed later.

For $\text{COA}_{S,C}$ and $\text{COA}_{W,C}$, the mean relative sensitivities are 1 by definition, though uncertainties are still calculated due to non-zero a values, while the reference profile utilised for $\text{CSOA}_{W,C}$, ensures that $\text{CSOA}_{W,C}$ $\text{CSOA}_{S,C}$ will have similar sensitivities. Interestingly, the distribution of the sensitivities, of $\text{COA}_{S,C}$, $\text{COA}_{W,C}$, and $\text{CSOA}_{W,C}$ in Figs. S32 and S33 is clearly multi-modal despite a -value constraints (although the overall $\text{COA}_{S,C}$ and $\text{COA}_{W,C}$ distributions remain relatively narrow), but the reason for this is unknown.

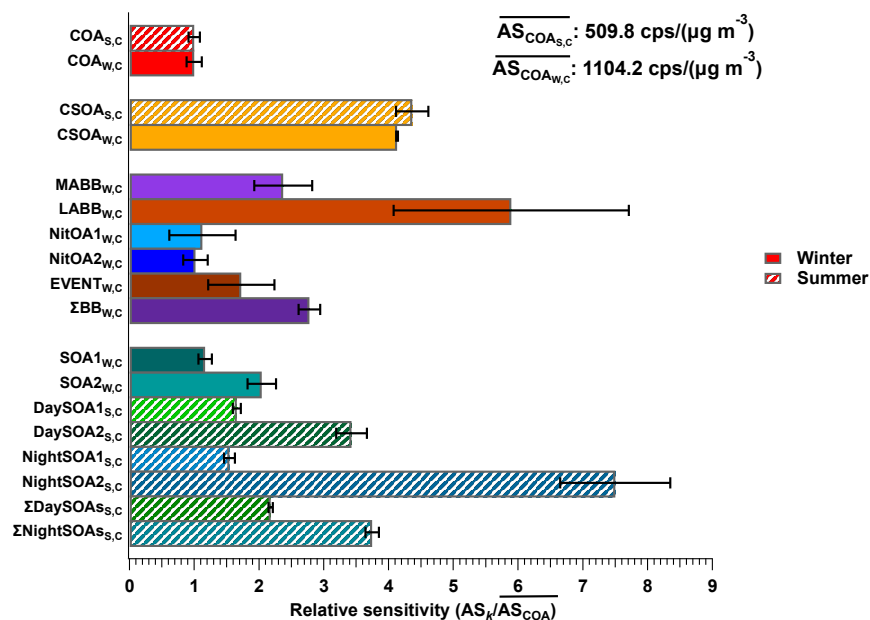
1 The next group of factors ($LABB_{w,c}$, $MABB_{w,c}$, $NitOA1_{w,c}$, $NitOA2_{w,c}$ and $EVENT_{w,c}$) includes non-
2 negligible contributions from levoglucosan ($C_6H_{10}O_5$), produced typically from biomass-burning(BB)-
3 related activities. Previous work has demonstrated that the EESI-TOF sensitivity to levoglucosan is
4 higher than that of many other compounds and bulk SOA from representative precursors (Lopez-
5 Hilfiker et al., 2019; Brown et al., 2021). Indeed, although the set of studied compounds is far from
6 comprehensive, the relative sensitivity of the EESI-TOF to levoglucosan is among the highest yet
7 recorded. Therefore, despite the variation in composition of the POA-influenced factors, the effect of
8 the $C_6H_{10}O_5$ content on the overall factor sensitivity is often considerable for cases where this ion is
9 strongly influenced by levoglucosan. Figure 6 shows AS_k as a function of the $C_6H_{10}O_5$ fraction for all
10 factors for which the $C_6H_{10}O_5$ signal is believed to result largely from levoglucosan. This analysis
11 accounts for all factors resolved from the cPMF of the winter dataset except $CSOA_{w,c}$, because
12 $CSOA_{w,c}$ is dominated by the signal from the protonated nicotine ($[C_{10}H_{14}N_2]H^+$) ion, which is both
13 chemically different (reduced nitrogen) and has a different ionisation pathway than other measured ions.
14 The four summer SOA factors are excluded as well, because the contribution from $C_6H_{10}O_5$ in these
15 factors was previously attributed to terpene and/or aromatic oxidation products (Stefenelli et al., 2019).
16 An obvious qualitative trend of increasing sensitivity with increasing levoglucosan fraction is evident
17 with Pearson r^2 of 0.676, indicating the overwhelming influence of the high sensitivity species
18 levoglucosan on the factor apparent sensitivity.

19 For the primary BB-related factors, the uncertainties are generally higher than for the other factors (see
20 Fig. S36). In contrast, the aggregated BB factor ($\Sigma BB_{w,c}$, and $\Sigma BB_{w,c} = MABB_{w,c} + LABB_{w,c} +$
21 $NitOA1_{w,c} + NitOA2_{w,c} + EVENT_{w,c}$) is less uncertain and has a narrower sensitivity distribution. This
22 suggests that the overall classification of signal as biomass burning-related is robust, but the subdivision
23 into more specific BB-related sources carries higher uncertainties. Likewise, the relative sensitivities of
24 $\Sigma DaySOAs_{s,c}$ and $\Sigma NightSOAs_{s,c}$ are less uncertain compared to individual corresponding SOA factors
25 in summer (as shown in Fig. S35). This contrast suggests that coarse classifications of factors may have
26 higher precision, but provide less information, whereas fine classifications of factors may have higher
27 uncertainties, but potentially provide more information from each factor. It also suggests that, at least
28 for these datasets, factor mixing occurs primarily between factors with closely related sources. Despite
29 their higher uncertainties, the finest classification levels explored here still appear to be meaningful. We
30 also note that both datasets investigated here are of relatively short duration, and factor separation may
31 improve in longer datasets.

32 The final group of factors in Fig. 5 corresponds to SOA. The relative sensitivities of the SOA factors in
33 winter are shown to be lower than any of the SOA factors resolved during summer. This is consistent
34 with expectations regarding the seasonal differences in the dominant SOA precursors and the expected
35 AS_k of the resulting SOA. At this site, SOA precursors are expected to be dominated by monoterpenes
36 in summer, and biomass burning (increasing the contribution of phenols, naphthalenes, and other
37 aromatics) in winter, with traffic making a lesser contribution in both seasons (Daellenbach et al., 2016;
38 Qi et al., 2020). This is supported by analysis of the characteristics of the retrieved factors as discussed
39 above (Qi et al., 2019; Stefenelli et al., 2019). Previous studies have shown differences in the EESI-
40 TOF bulk sensitivity to SOA from different precursors, with terpene-derived SOA generally exhibiting
41 higher sensitivity than SOA from light aromatics (Lopez-Hilfiker et al., 2019; Wang et al., 2021). Figure
42 7 shows the AS/AS_{COA} for two $DaySOAs_{s,c}$ and $NightSOAs_{s,c}$ factors in summer, as well as the
43 $\Sigma DaySOAs_{s,c}$ and $\Sigma NightSOAs_{s,c}$, which are the aggregates of the individual $DaySOAs_{s,c}$ and
44 $NightSOAs_{s,c}$ factors ($\Sigma DaySOAs_{s,c} = DaySOA1_{s,c} + DaySOA2_{s,c}$; and $\Sigma NightSOAs_{s,c} =$
45 $NightSOA1_{s,c} + NightSOA2_{s,c}$), respectively, and two $SOA_{w,c}$ factors in winter as a function of their
46 H:C ratio calculated from the EESI-TOF component. A trend of increasing sensitivity with increasing

1 H:C ratio is observed for the summer SOAs and winter SOAs ($SOA_{1w,c}$ and $SOA_{2w,c}$), with an overall
 2 Spearman's rank correlation of 0.833. Consistent with Wang et al. (2021), H:C is found to be a better
 3 predictor of AS_k than either O:C or OSc, yielding Spearman's rank correlation of 0.833 for AS_k vs. H:C,
 4 -0.167 for AS_k vs. O:C, and -0.452 for AS_k vs. OSc (Fig. S37a and Fig. S37b).

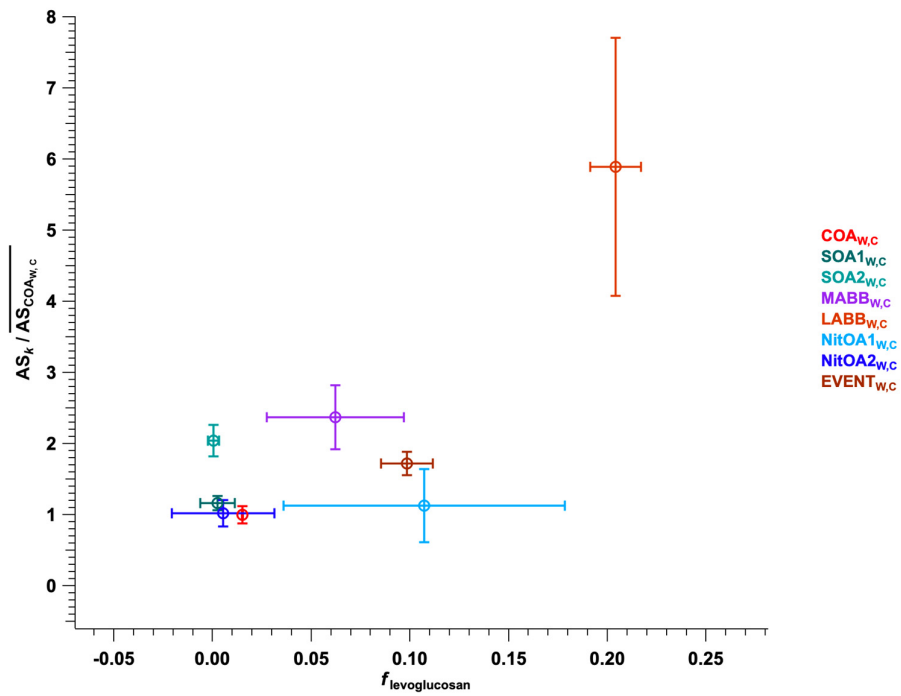
5 For the SOA factors, we compare AS_k retrieved to AS_k predicted using a molecular formula-based
 6 parameterisation trained with laboratory SOA measurements, as described in Sect. 2.2.3 (Wang et al.,
 7 2021). No parameterisations presently exist for POA factors, so these are excluded from the comparison,
 8 although to allow comparison between campaigns the model is used to calculate a reference value for
 9 AS_{COA} . Figure 8 compares the AS_k values based on model predictions against values determined from
 10 cPMF. For summer SOAs, the LMN (limonene)-based parameterisation is applied as a surrogate for
 11 terpene oxidation products. Regarding the winter SOAs, three scenarios (cresol, LMN and TMB) are
 12 applied, as the winter SOAs in Zurich are mainly related to oxidation of biomass burning emissions,
 13 which include monoterpenes, phenols, naphthalenes, and other aromatics (Rouvière et al., 2006; Bruns
 14 et al., 2016; Kelly et al., 2018). In Fig. 8, 1:1, 1:2, 1:4, and 1:8 lines are provided to guide the eye,
 15 although a 1:1 correspondence is not expected because the models are not trained on primary COA. The
 16 figure shows a monotonic increase in model sensitivity predictions with increasing cPMF-derived
 17 sensitivities, with the sole exception of $SOA_{2w,c}$. Specifically, the summer-derived points fall mainly
 18 between the 1:1 and 1:2 lines, while for $SOA_{1w,c}$, the model predictions are roughly a factor of 2 lower
 19 relative to the cPMF results. This offset may reflect differences in the appropriateness of the selected
 20 precursor surrogate. The $SOA_{2w,c}$ factor is a slight outlier, probably because the AS_k for this factor is
 21 more uncertain than the others (and not fully captured by the error bars in Fig. 5) due to the high
 22 contribution from inorganic nitrate (~80 % of mass) in its factor profile. Given the limitations of the
 23 multi-variate parameterisation (see Sect. 2.2.3) and the several orders of magnitude variation in EESI-
 24 TOF sensitivities to individual compounds, the qualitative agreement between AS_k values independently
 25 retrieved from multivariate parameterisation and cPMF provide support for both methods.



26

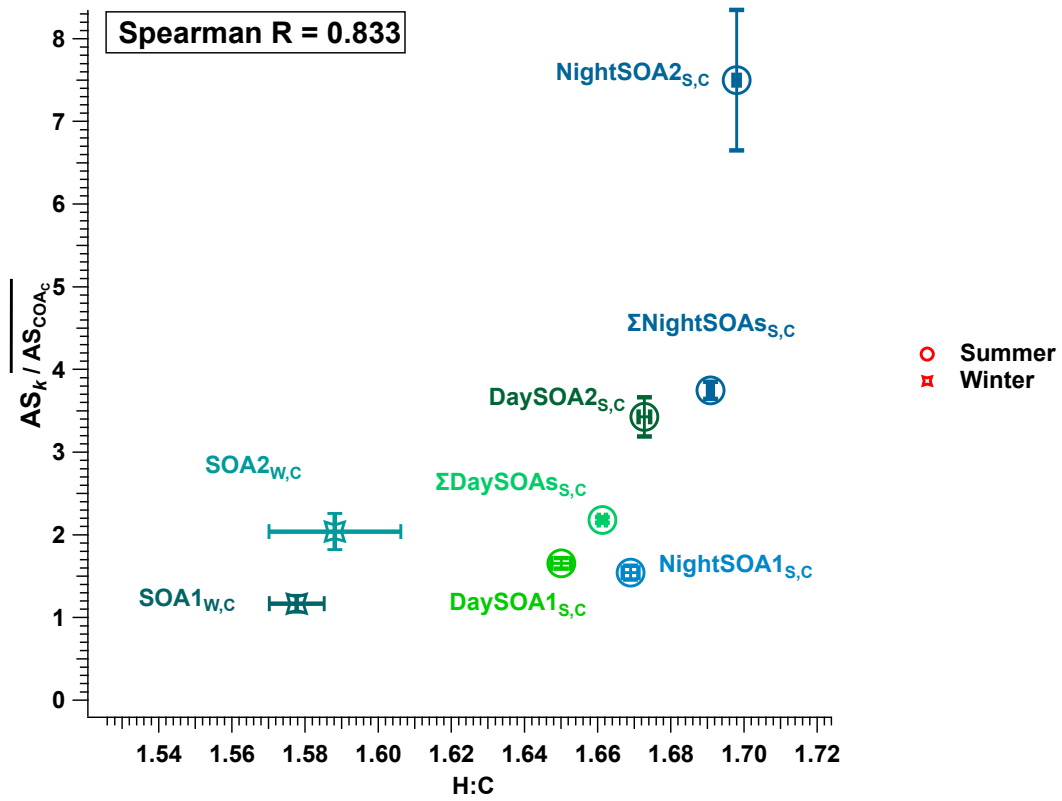
27 Figure 5. Comparison of AS_k / AS_{COA} of different factors resolved from the cPMF on the summer and
 28 winter datasets. Mean values are shown as bars, and error bars indicate the standard deviation over all
 29 accepted bootstrap runs. The following factor aggregations are also shown: $\Sigma BB_{w,c} = MABB_{w,c} +$

- 1 $LABB_{w,c} + NitOA1_{w,c} + NitOA2_{w,c} + EVENT_{w,c}; \Sigma DaySOAs_{s,c} = DaySOA1_{s,c} + DaySOA2_{s,c};$
- 2 and $\Sigma NightSOAs_{s,c} = NightSOA1_{s,c} + NightSOA2_{s,c}.$



- 3
- 4 Figure 6. Relative apparent sensitivity $AS_k / AS_{COA_{w,c}}$ as a function of levoglucosan fraction for all
- 5 factors resolved from the cPMF of the winter dataset except $CSOA_{w,c}$. Error bars denote standard
- 6 deviation.

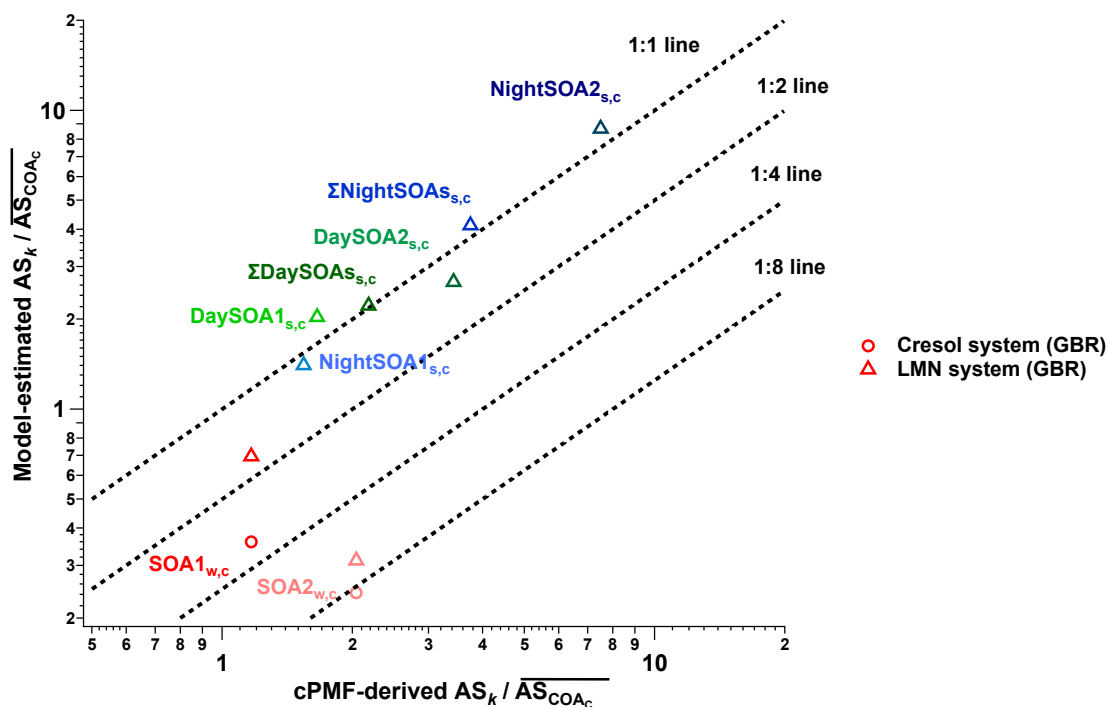
1



2

3 Figure 7. AS_k / AS_{COAc} of SOA factors retrieved from the summer and winter datasets as a function of
4 the H:C ratio. Error bars denote standard deviation across all accepted runs. Spearman correlation is
5 0.833, as indicated in the top-left corner.

1



2

3 Figure 8. The estimated relative apparent sensitivity to COA ($AS_k / \overline{AS}_{COAc}$) from the gradient boosting
 4 regression (GBR) model as a function of cPMF-derived $AS_k / \overline{AS}_{COAc}$. The symbols indicate the
 5 different oxidation-precursor system (LMN for SOA produced from oxidation of limonene by ozone,
 6 cresol and TMB for SOA produced from oxidation of *o*-cresol and 1,3,5-trimethylbenzene by OH
 7 radicals, respectively).

8

9

10 4. Atmospheric implications

11

12 The application of factor-dependent sensitivities can qualitatively and quantitatively affect the source
 13 apportionment results. Figures 9a and 9b compare the source apportionment results from cPMF on the
 14 summer and winter datasets using the calculated factor sensitivities (AS_k) (i.e., direct outputs of the
 15 cPMF analysis) vs. using a single bulk sensitivity (AS_{bulk}) for all factors, where the latter is calculated
 16 as the ratio of the total OA measured by the EESI-TOF (cps) to that measured by the AMS ($\mu\text{g m}^{-3}$).
 17 Figures 10a and 10b compare the total OA concentrations returned from the cPMF using AS_k and
 18 AS_{bulk} to the total OA measured by the AMS. Table S3 summarises the retrieved AS_k values for each
 19 factor (note that although the relative AS_k are believed to be intrinsic properties of the factors, the
 20 absolute sensitivities are instrument- and tuning-dependent, and will vary between campaigns).

21

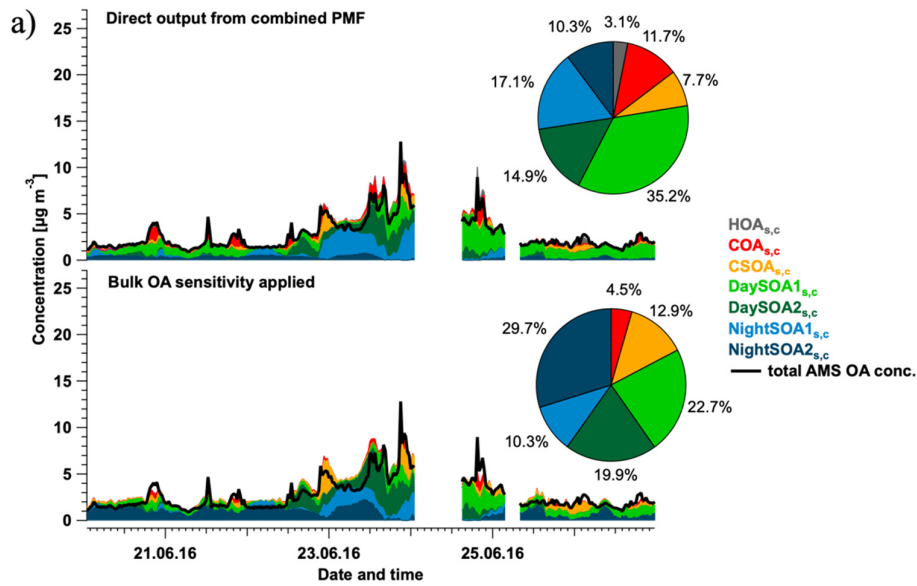
22 In the Zurich summer campaign, the bulk OA sensitivity $AS_{bulk_{S,C}}$ ($1254.0 \text{ cps } (\mu\text{g m}^{-3})^{-1}$) is higher than
 23 that of $AS_{COA_{S,C}}$ ($509.8 \text{ cps } (\mu\text{g m}^{-3})^{-1}$). Four factors ($HOA_{S,C}$, $COA_{S,C}$, $DaySOA1_{S,C}$ and $NightSOA1_{S,C}$)
 24 are underestimated, whereas three factors ($CSOA_{S,C}$, $DaySOA2_{S,C}$ and $NightSOA2_{S,C}$) are
 25 overestimated when $AS_{bulk_{S,C}}$ is used. Using the calculated AS_k , the contribution of $COA_{S,C}$ to total OA
 26 more than doubles, from 4.5 % to 11.7 % as shown in Fig. 9a). Similarly, the application of AS_k increases
 27 the contributions of $DaySOA1_{S,C}$ and $NightSOA1_{S,C}$ from 22.7 % to 35.2 %, and from 10.3 % to 17.1 %, respectively. Among the overestimated factors, the largest decrease post-correction is found for

1 NightSOA_{2s,c}, the contribution of which decreases by approximately a factor of three (from 29.7 % to
2 10.3%). Smaller post-correction decreases are observed for the contributions of CSOA_{s,c} (12.9 % to
3 7.7 %) and DaySOA_{2s,c} (19.9 % to 14.9 %). If factor-dependent sensitivities were ignored,
4 NightSOA_{2s,c} would be the largest contributor to total OA, followed by DaySOA_{1s,c} whereas the full
5 analysis indicates that DaySOA_{1s,c} is the largest contributor.

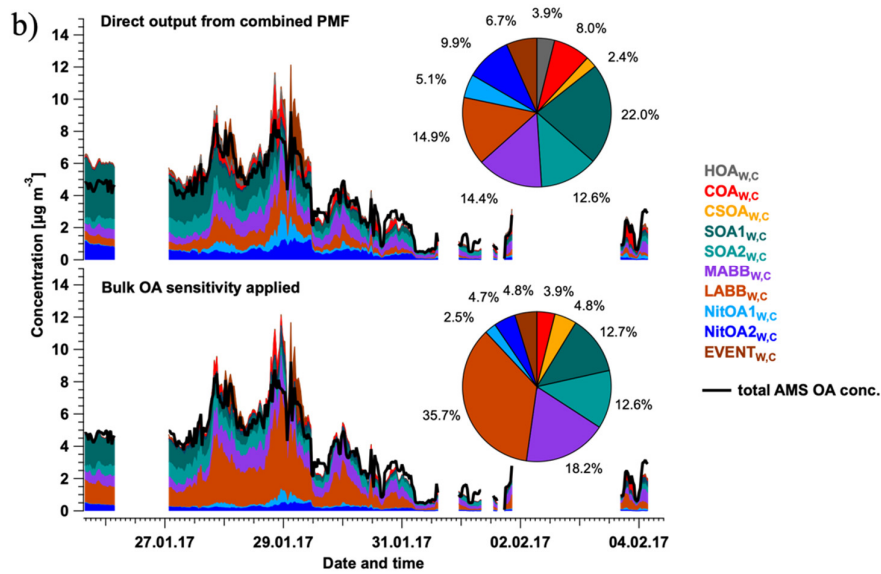
6
7 Similar to the summer campaign, application of AS_k significantly affects the source apportionment
8 results in winter. CSOA_{w,c}, MABB_{w,c}, and LABB_{w,c} are shown to be overestimated, while HOA_{w,c},
9 COA_{w,c}, SOA_{1w,c}, NitOA_{1w,c}, NitOA_{2w,c} and EVENT_{w,c} are underestimated. If factor-dependent
10 sensitivities were not considered, LABB_{w,c} and MABB_{w,c} would appear to be the dominant
11 contributors to total OA (35.7 % and 18.2 % respectively) due to their high levoglucosan content.
12 However, the full cPMF analysis indicates the LABB_{w,c} and MABB_{w,c} contributions to be 14.9 % and
13 14.4 %, respectively, whereas accounting for AS_k increases the contribution of SOA_{1w,c} from 12.7 %
14 to 22.0 %, making it the largest contributor.

15
16 For both the summer and winter datasets, calculation of total OA from cPMF results using factor-
17 specific AS_k significantly outperforms that using a single AS_{bulk} . This is evident from an increased r^2
18 (0.966 vs 0.821) for summer. However, the r^2 is similar between the two approaches in winter (0.947
19 vs 0.943). The difference after applying AS_k and AS_{bulk} in r^2 might be related to the extent to which
20 the contribution from factors with high AS_k and low AS_k to total OA changes over the time during the
21 campaign, which can vary in different datasets.

22
23 Box-and-whisker diagrams of factor contributions to total OA with/without applying AS_k values for
24 summer and winter are presented in Fig. 11. In the Zurich summer campaign, the box plots of the
25 corrected contributions of all six factors fall completely outside of the interquartile range (IQR) of the
26 uncorrected results, suggesting that the use of a single AS_{bulk} would lead to significant biases. In contrast,
27 the winter campaign exhibits a lack of overlap between the AS_k and AS_{bulk} -derived results for eight
28 factors (HOA_{w,c}, COA_{w,c}, CSOA_{w,c}, SOA_{1w,c}, SOA_{2w,c}, NitOA_{1w,c}, NitOA_{2w,c} and EVENT_{w,c}),
29 whereas two factors overlap (SOA_{2w,c} and MABB_{w,c}). This may result from statistical uncertainties
30 in bootstrap analysis coupled with a less robust division between certain factors, yielding a wide
31 distribution, e.g., MABB_{w,c}, and/or AS_k values that are similar to AS_{bulk} (2271.1 cps ($\mu\text{g m}^{-3}$)⁻¹), e.g.,
32 SOA_{2w,c} (2253.2 cps ($\mu\text{g m}^{-3}$)⁻¹), and MABB_{w,c} (2619.0 cps ($\mu\text{g m}^{-3}$)⁻¹).

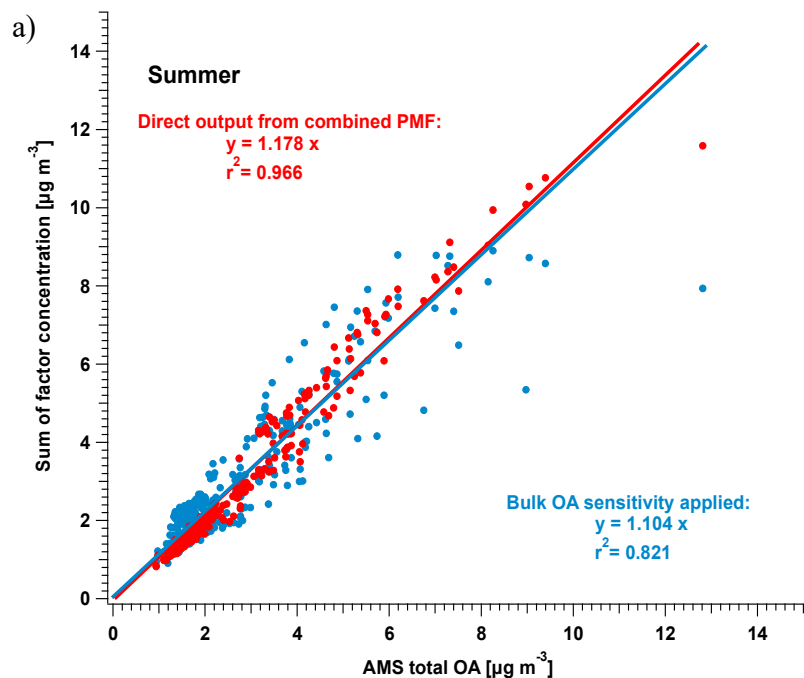


1

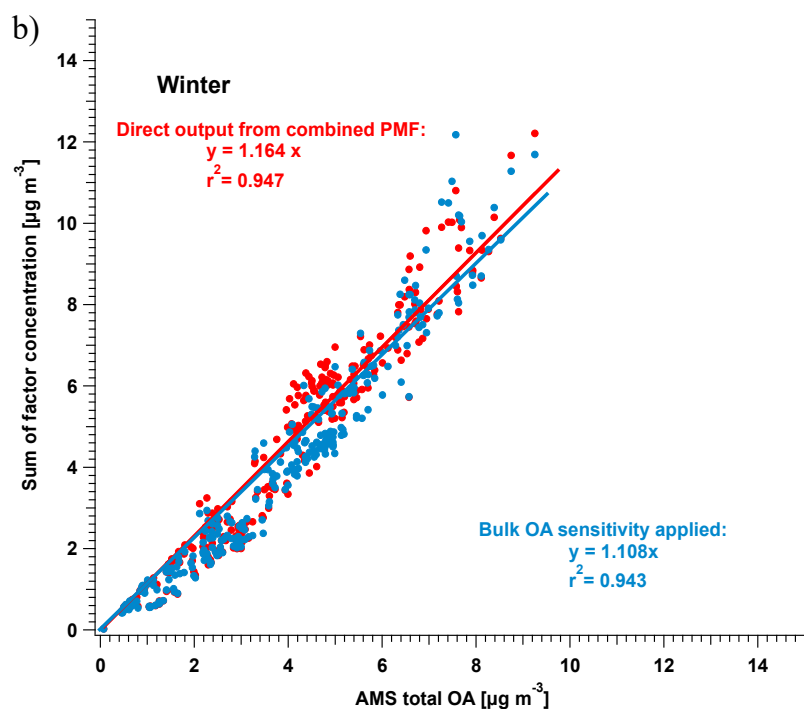


2

3 Figure 9. Comparison of source apportionment results between direct output from cPMF (i.e.,
 4 accounting for factor-dependent sensitivities) and application of a single bulk OA sensitivity, applied
 5 to the Zurich summer (a) and winter (b) datasets. Stack plots of factor time series directly from
 6 combined PMF and factor time series calculated from bulk OA sensitivity compared with total AMS
 7 OA concentration are shown in the upper and lower panel, respectively in each subfigure, together with
 8 the corresponding factor contribution shown in the pie chart. Note that here the contribution of the
 9 InorgNit factor and the contributions of NO^+ and NO_2^+ from inorganic nitrate in each factor are excluded
 10 to account only for the total OA.



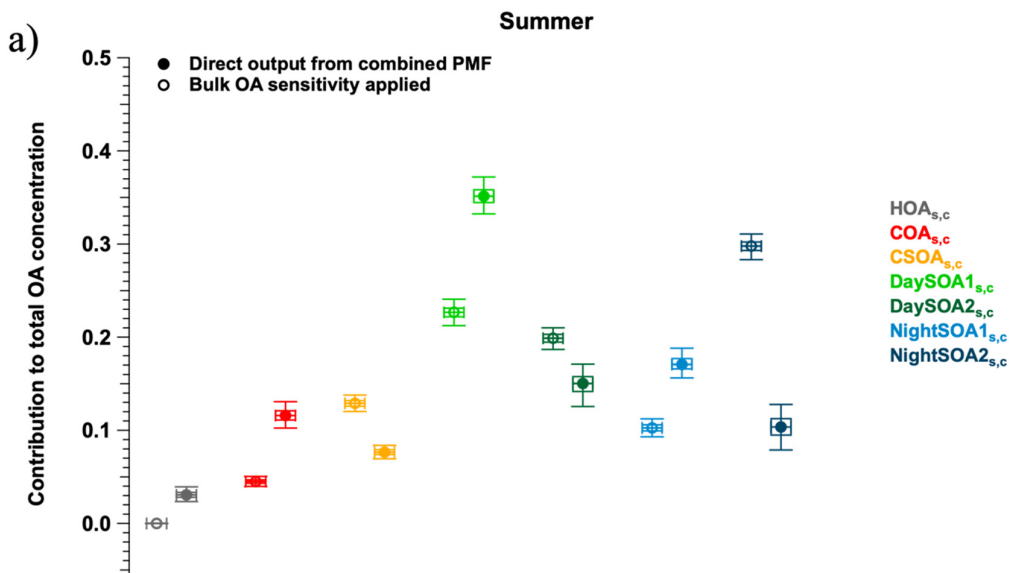
1



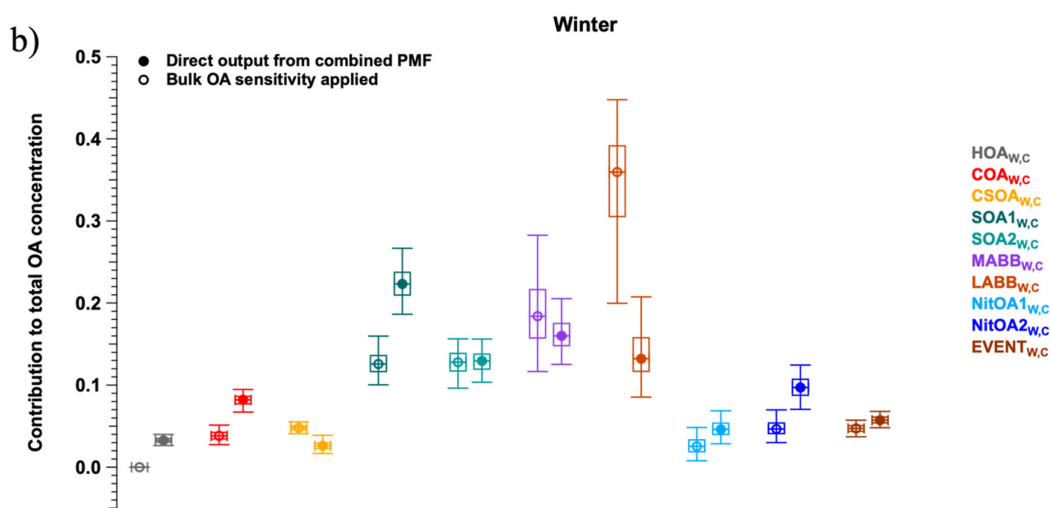
2

3 Figure 10. Comparison between the sum of factor concentrations in each time point with (in red) and
 4 without (in blue) taking the factor-dependent sensitivity into account and total OA measured by AMS
 5 for summer in a) and winter in b). A linear fit is conducted based on the Levenberg-Marquardt least
 6 orthogonal distance method. Note that here the contribution of the InorgNit factor and the contributions
 7 of NO^+ and NO_2^+ from inorganic nitrate in each factor are excluded.

8



1



2

3

4 Figure 11. Box-and-whisker diagrams of factor contributions to total OA with/without applying the
 5 factor dependent sensitivities, for summer in a) and winter in b) within accepted solutions. For each pair
 6 of factors, the contribution without factor-dependent sensitivity applied is shown in the left box (open
 7 symbols), whereas the contribution corrected by factor-dependent sensitivity is shown in the right box
 8 (filled symbols). The box-and-whisker diagram shows the mean (open/filled circle), median (horizontal
 9 bar), interquartile range (rectangle, the 25th percentile is the lower edge and the 75th is the upper edge),
 10 and minimum/maximum values (whiskers). Note that here the contribution of InorgNit factor and
 11 contribution of NO⁺ and NO₂⁺ from inorganic nitrate in each factor are excluded.

12

5. Conclusions

We address the longstanding challenges in achieving quantitative source apportionment of SOA sources by conducting a positive matrix factorisation (PMF) analysis of a dataset combining measurements from an aerosol mass spectrometer (AMS) and an extractive electrospray ionisation time-of-flight mass spectrometer (EESI-TOF). This approach combines the strengths of the two instruments, namely the quantification ability of the AMS and the chemical resolution of the EESI-TOF. We demonstrate the utility of this approach by PMF analysis of combined EESI-TOF/AMS datasets collected during summer and winter in Zurich, Switzerland. The results retain the chemical resolution of the standalone EESI-TOF PMF, while additionally providing quantitative factor time series and the EESI-TOF bulk sensitivity to different OA factors.

Note that while these methods provide a general procedure for cPMF analysis, the specific parameters employed (i.e., the number of factors (p), instrument weighting parameter (C_{inst}), and the factors to be constrained and the tightness of constraints (a value ranges)) are dataset-specific and should be determined independently for each new analysis.

The cPMF method intrinsically provides factor-dependent sensitivities ($\text{cps} (\mu\text{g m}^{-3})^{-1}$) for the EESI-TOF. To account for organonitrate content, the AMS ions NO^+ and NO_2^+ are included in the cPMF analysis. Organic and inorganic contributions to these ions are estimated on a factor-by-factor basis using the method of Kiendler-Scharr et al. (2016).

For practical reasons, sensitivities between winter and summer campaigns are compared using cooking-related OA (COA) as a common reference. The retrieved factor sensitivities range from approximately 1.3 to 7.5 times the sensitivity of COA. The relative sensitivities of SOA factors are precursor-dependent, and qualitatively consistent with trends observed in lab measurements of SOA from single precursors (Lopez-Hilfiker et al., 2019). The SOA sensitivities estimated using our cPMF approach also agree with the sensitivities predicted by multi-variate regression models (Wang et al., 2021), which further demonstrates that SOA sensitivities are precursor- and/or source-dependent. Comparison of source apportionment results using factor-dependent sensitivities to uncorrected results show substantial differences, highlighting the importance of quantitative analysis. For example, before applying factor-dependent sensitivities, the contribution of a daytime SOA factor is underestimated by about 30 % (22.7 % before vs 35.2 % after), whereas the contribution of a nighttime SOA factor is almost overestimated by a factor of 3 in the summer campaign (29.7 % before vs 10.3 % after). As for the winter campaign, the contribution of less-aged biomass burning factor to total OA in Zurich winter dataset is 35.7 %, making it a major factor in winter without considering its factor-dependent sensitivity. However, this factor is significantly overestimated by more than a factor of 2 (35.7 %, before vs 14.9 % after). In contrast, the SOA1 factor in winter is underestimated, with its contribution increasing from 12.7% to 22.0 %.

These considerable differences in the source contributions between the uncorrected EESI-TOF and cPMF results highlight the challenges in interpreting standalone source apportionment results for instruments where ion-specific sensitivity information is not readily available, such as EESI-TOF or FIGAERO-CIMS. Although the time trends of such analyses are likely robust, interpretation of the relative composition requires caution. Therefore, if such interpretation is desired, it is advised to employ analysis strategies such as cPMF that are capable of integrating quantitative measurements from reference instruments.

1 The cPMF method presented herein can be utilised as-is not only for the AMS/EESI-TOF combination,
2 but to any dataset comprising data from multiple instruments. As such, it provides a promising strategy
3 for utilising instruments with high chemical resolution but semi-quantitative performance (i.e., a linear
4 but hard-to-calibrate response to mass) within the framework of a quantitative source apportionment.

5

6

7 *Data Availability.* The data presented in the text and figures will be available at the Zenodo Online repository
8 (<https://zenodo.org>) upon final publication.

9 *Competing interests.* The authors declare that they have no conflict of interest.

10 *Author contributions.* GS and LQ conducted the campaigns in summer and winter in Zurich, respectively. YT
11 performed the whole analysis. DSW performed the multi-variate model for machine learning parameterisation of
12 sensitivities. FC developed the weighting and constraining functions in SoFi. JGS conceived and supervised the
13 project. All authors currently working at PSI contributed to the data interpretation. All authors contributed to the
14 manuscript revision.

15 *Acknowledgements.* We gratefully acknowledge the contribution from Dr. Anna Tobler and Mr. Gang Chen for
16 coordinating the workstation for the computationally-intensive bootstrap analysis.

17 *Financial support.* This project has received funding from the Swiss National Science Foundation (grant no.
18 BSSGI0_155846) and the European Union's Horizon 2020 Research and Innovation Program under the Marie
19 Skłodowska-Curie grant agreement no. 701647.

20

21

22

1 Reference

- 2 Alfarra, M. R., Prevot, A. S. H., Szidat, S., Sandradewi, J., Weimer, S., Lanz, V. A., Schreiber, D.,
3 Mohr, M., and Baltensperger, U.: Identification of the mass spectral signature of organic aerosols
4 from wood burning emissions, *Environ. Sci. Technol.*, 41, 5770-5777,
5 <https://doi.org/10.1021/es062289b>, 2007.
- 6 Allan, J. D., Jimenez, J. L., Williams, P. I., Alfarra, M. R., Bower, K. N., Jayne, J. T., Coe, H., and
7 Worsnop, D. R.: Quantitative sampling using an Aerodyne aerosol mass spectrometer: 1. Techniques
8 of data interpretation and error analysis (vol 108, art no 4090, 2003), *J. Geophys. Res. Atmos.*, 108,
9 4090, <https://doi.org/10.1029/2002JD002358>, 2003.
- 10 Beelen, R., Raaschou-Nielsen, O., Stafoggia, M., Andersen, Z. J., Weinmayr, G., Hoffmann, B., Wolf,
11 K., Samoli, E., Fischer, P., Nieuwenhuijsen, M., Vineis, P., Xun, W. W., Katsouyanni, K.,
12 Dimakopoulou, K., Oudin, A., Forsberg, B., Modig, L., Havulinna, A. S., Lanki, T., Turunen, A.,
13 Oftedal, B., Nystad, W., Nafstad, P., De Faire, U., Pedersen, N. L., Ostenson, C. G., Fratiglioni, L.,
14 Penell, J., Korek, M., Pershagen, G., Eriksen, K. T., Overvad, K., Ellermann, T., Eeftens, M., Peeters,
15 P. H., Meliefste, K., Wang, M., Bueno-de-Mesquita, B., Sugiri, D., Kramer, U., Heinrich, J., de
16 Hoogh, K., Key, T., Peters, A., Hampel, R., Concin, H., Nagel, G., Ineichen, A., Schaffner, E., Probst-
17 Hensch, N., Kunzli, N., Schindler, C., Schikowski, T., Adam, M., Phuleria, H., Vilier, A., Clavel-
18 Chapelon, F., Declercq, C., Grioni, S., Krogh, V., Tsai, M. Y., Ricceri, F., Sacerdote, C., Galassi, C.,
19 Migliore, E., Ranzi, A., Cesaroni, G., Badaloni, C., Forastiere, F., Tamayo, I., Amiano, P.,
20 Dorronsoro, M., Katsoulis, M., Trichopoulou, A., Brunekreef, B., and Hoek, G.: Effects of long-term
21 exposure to air pollution on natural-cause mortality: an analysis of 22 European cohorts within the
22 multicentre ESCAPE project, *Lancet*, 383, 785-795, [https://doi.org/10.1016/S0140-6736\(13\)62158-3](https://doi.org/10.1016/S0140-6736(13)62158-3),
23 2014.
- 24 Bi, C., Krechmer, J. E., Frazier, G. O., Xu, W., Lambe, A. T., Claflin, M. S., Lerner, B. M., Jayne, J.
25 T., Worsnop, D. R., Canagaratna, M. R., and Isaacman-VanWertz, G.: Quantification of isomer-
26 resolved iodide chemical ionization mass spectrometry sensitivity and uncertainty using a voltage-
27 scanning approach, *Atmos. Meas. Tech.*, 14, 6835-6850, <https://doi.org/10.5194/amt-14-6835-2021>,
28 2021.
- 29 Brown, W. L., Day, D. A., Stark, H., Pagonis, D., Krechmer, J. E., Liu, X., Price, D. J., Katz, E. F.,
30 DeCarlo, P. F., Masoud, C. G., Wang, D. S., Hildebrandt Ruiz, L., Arata, C., Lunderberg, D. M.,
31 Goldstein, A. H., Farmer, D. K., Vance, M. E., and Jimenez, J. L.: Real-time organic aerosol chemical
32 speciation in the indoor environment using extractive electrospray ionization mass spectrometry,
33 *Indoor Air*, 31, 141-155, <https://doi.org/10.1111/ina.12721>, 2021.
- 34 Bruns, E. A., El Haddad, I., Slowik, J. G., Kilic, D., Klein, F., Baltensperger, U., and Prévôt, A. S. H.:
35 Identification of significant precursor gases of secondary organic aerosols from residential wood
36 combustion, *Scientific Reports*, 6, 27881, <https://doi.org/10.1038/srep27881>, 2016.
- 37 Canagaratna, M. R., Jayne, J. T., Jimenez, J. L., Allan, J. D., Alfarra, M. R., Zhang, Q., Onasch, T. B.,
38 Drewnick, F., Coe, H., Middlebrook, A., Delia, A., Williams, L. R., Trimborn, A. M., Northway, M.
39 J., DeCarlo, P. F., Kolb, C. E., Davidovits, P., and Worsnop, D. R.: Chemical and microphysical
40 characterization of ambient aerosols with the aerodyne aerosol mass spectrometer, *Mass Spectrom.*
41 *Rev.*, 26, 185-222, <https://doi.org/10.1002/mas.20115>, 2007.
- 42 Canonaco, F., Crippa, M., Slowik, J. G., Baltensperger, U., and Prevot, A. S. H.: SoFi, an IGOR-
43 based interface for the efficient use of the generalized multilinear engine (ME-2) for the source
44 apportionment: ME-2 application to aerosol mass spectrometer data, *Atmos. Meas. Tech.*, 6, 3649-
45 3661, <https://doi.org/10.5194/amt-6-3649-2013>, 2013.
- 46 Canonaco, F., Tobler, A., Chen, G., Sosedova, Y., Slowik, J. G., Bozzetti, C., Daellenbach, K. R., El
47 Haddad, I., Crippa, M., Huang, R. J., Furger, M., Baltensperger, U., and Prévôt, A. S. H.: A new
48 method for long-term source apportionment with time-dependent factor profiles and uncertainty
49 assessment using SoFi Pro: application to 1 year of organic aerosol data, *Atmos. Meas. Tech.*, 14,
50 923-943, <https://doi.org/10.5194/amt-14-923-2021>, 2021.
- 51 Chen, Y., Takeuchi, M., Nah, T., Xu, L., Canagaratna, M. R., Stark, H., Baumann, K., Canonaco, F.,
52 Prévôt, A. S. H., Huey, L. G., Weber, R. J., and Ng, N. L.: Chemical characterization of secondary
53 organic aerosol at a rural site in the southeastern US: insights from simultaneous high-resolution time-
54 of-flight aerosol mass spectrometer (HR-ToF-AMS) and FIGAERO chemical ionization mass

1 spectrometer (CIMS) measurements, *Atmos. Chem. Phys.*, 20, 8421-8440,
2 <https://doi.org/10.5194/acp-20-8421-2020>, 2020.

3 Chow, J. C., Bachmann, J. D., Wierman, S. S. G., Mathai, C. V., Malm, W. C., White, W. H.,
4 Mueller, P. K., Kumar, N., and Watson, J. G.: Visibility: Science and regulation - Discussion, *J. Air*
5 *Waste Manag. Assoc.*, 52, 973-999, <https://doi.org/10.1016/j.atmosenv.2010.09.060>, 2002.

6 Crippa, M., Canonaco, F., Slowik, J. G., El Haddad, I., DeCarlo, P. F., Mohr, C., Heringa, M. F.,
7 Chirico, R., Marchand, N., Temime-Roussel, B., Abidi, E., Poulain, L., Wiedensohler, A.,
8 Baltensperger, U., and Prévôt, A. S. H.: Primary and secondary organic aerosol origin by combined
9 gas-particle phase source apportionment, *Atmos. Chem. Phys.*, 13, 8411-8426,
10 <https://doi.org/10.5194/acp-13-8411-2013>, 2013a.

11 Crippa, M., El Haddad, I., Slowik, J. G., DeCarlo, P. F., Mohr, C., Heringa, M. F., Chirico, R.,
12 Marchand, N., Sciare, J., Baltensperger, U., and Prévôt, A. S. H.: Identification of marine and
13 continental aerosol sources in Paris using high resolution aerosol mass spectrometry, *J. Geophys. Res.*
14 *Atmos.*, 118, 1950-1963, <https://doi.org/10.1002/jgrd.50151>, 2013b.

15 Crippa, M., Canonaco, F., Lanz, V. A., Aijala, M., Allan, J. D., Carbone, S., Capes, G., Ceburnis, D.,
16 Dall'Osto, M., Day, D. A., DeCarlo, P. F., Ehn, M., Eriksson, A., Freney, E., Hildebrandt Ruiz, L.,
17 Hillamo, R., Jimenez, J. L., Junninen, H., Kiendler-Scharr, A., Kortelainen, A. M., Kulmala, M.,
18 Laaksonen, A., Mensah, A., Mohr, C., Nemitz, E., O'Dowd, C., Ovadnevaite, J., Pandis, S. N., Petaja,
19 T., Poulain, L., Saarikoski, S., Sellegri, K., Swietlicki, E., Tiitta, P., Worsnop, D. R., Baltensperger,
20 U., and Prevot, A. S. H.: Organic aerosol components derived from 25 AMS data sets across Europe
21 using a consistent ME-2 based source apportionment approach, *Atmos. Chem. Phys.*, 14, 6159-6176,
22 <https://doi.org/10.5194/acp-14-6159-2014>, 2014.

23 Daellenbach, K. R., Bozzetti, C., Krepelova, A. K., Canonaco, F., Wolf, R., Zotter, P., Fermo, P.,
24 Crippa, M., Slowik, J. G., Sosedova, Y., Zhang, Y., Huang, R. J., Poulain, L., Szidat, S.,
25 Baltensperger, U., El Haddad, I., and Prevot, A. S. H.: Characterization and source apportionment of
26 organic aerosol using offline aerosol mass spectrometry, *Atmos. Meas. Tech.*, 9, 23-39,
27 <https://doi.org/10.5194/amt-9-23-2016>, 2016.

28 Daellenbach, K. R., Stefenelli, G., Bozzetti, C., Vlachou, A., Fermo, P., Gonzalez, R., Piazzalunga,
29 A., Colombi, C., Canonaco, F., Hueglin, C., Kasper-Giebl, A., Jaffrezo, J. L., Bianchi, F., Slowik, J.
30 G., Baltensperger, U., El-Haddad, I., and Prevot, A. S. H.: Long-term chemical analysis and organic
31 aerosol source apportionment at nine sites in central Europe: source identification and uncertainty
32 assessment, *Atmos. Chem. Phys.*, 17, 13265-13282, <https://doi.org/10.5194/acp-17-13265-2017>,
33 2017.

34 Daellenbach, K. R., Uzu, G., Jiang, J., Cassagnes, L.-E., Leni, Z., Vlachou, A., Stefenelli, G.,
35 Canonaco, F., Weber, S., Segers, A., Kuenen, J. J. P., Schaap, M., Favez, O., Albinet, A., Aksoyoglu,
36 S., Dommen, J., Baltensperger, U., Geiser, M., El Haddad, I., Jaffrezo, J.-L., and Prévôt, A. S. H.:
37 Sources of particulate-matter air pollution and its oxidative potential in Europe, *Nature*, 587, 414-419,
38 <https://doi.org/10.1038/s41586-020-2902-8>, 2020.

39 Davison, A. C., and Hinkley, D. V.: *Bootstrap methods and their application*, Cambridge University
40 Press, Cambridge, New York, NY, USA, 1997.

41 DeCarlo, P. F., Kimmel, J. R., Trimborn, A., Northway, M. J., Jayne, J. T., Aiken, A. C., Gonin, M.,
42 Fuhrer, K., Horvath, T., Docherty, K. S., Worsnop, D. R., and Jimenez, J. L.: Field-deployable, high-
43 resolution, time-of-flight aerosol mass spectrometer, *Anal. Chem.*, 78, 8281-8289,
44 <https://doi.org/10.1021/ac061249n>, 2006.

45 Elser, M., Huang, R. J., Wolf, R., Slowik, J. G., Wang, Q. Y., Canonaco, F., Li, G. H., Bozzetti, C.,
46 Daellenbach, K. R., Huang, Y., Zhang, R. J., Li, Z. Q., Cao, J. J., Baltensperger, U., El-Haddad, I.,
47 and Prevot, A. S. H.: New insights into PM_{2.5} chemical composition and sources in two major cities
48 in China during extreme haze events using aerosol mass spectrometry, *Atmos. Chem. Phys.*, 16, 3207-
49 3225, <https://doi.org/10.5194/acp-16-3207-2016>, 2016.

50 Farmer, D. K., Matsunaga, A., Docherty, K. S., Surratt, J. D., Seinfeld, J. H., Ziemann, P. J., and
51 Jimenez, J. L.: Response of an aerosol mass spectrometer to organonitrates and organosulfates and
52 implications for atmospheric chemistry, *Proc Natl Acad Sci U S A*, 107, 6670,
53 <https://doi.org/10.1073/pnas.0912340107>, 2010.

54 Faxon, C., Hammes, J., Le Breton, M., Pathak, R. K., and Hallquist, M.: Characterization of organic
55 nitrate constituents of secondary organic aerosol (SOA) from nitrate-radical-initiated oxidation of

1 limonene using high-resolution chemical ionization mass spectrometry, *Atmos. Chem. Phys.*, 18,
2 5467-5481, <https://doi.org/10.5194/acp-18-5467-2018>, 2018.

3 Fenger, J.: Urban air quality, *Atmos. Environ.*, 33, 4877-4900, [https://doi.org/10.1016/S1352-](https://doi.org/10.1016/S1352-2310(99)00290-3)
4 [2310\(99\)00290-3](https://doi.org/10.1016/S1352-2310(99)00290-3), 1999.

5 Forster, P., Ramaswamy, V., Artaxo, P., Berntsen, T., Betts, R., Fahey, D. W., Haywood, J., Lean, J.,
6 Lowe, D. C., and Myhre, G.: Changes in atmospheric constituents and in radiative forcing. Chapter 2,
7 in: *Climate Change 2007. The Physical Science Basis*, 2007.

8 Fuller, S. J., Wragg, F. P. H., Nutter, J., and Kalberer, M.: Comparison of on-line and off-line
9 methods to quantify reactive oxygen species (ROS) in atmospheric aerosols, *Atmos. Environ.*, 92, 97-
10 103, <https://doi.org/10.1016/j.atmosenv.2014.04.006>, 2014.

11 Halliwell, B., and Cross, C. E.: Oxygen-derived species: their relation to human disease and
12 environmental stress, *Environ Health Perspect*, 102 Suppl 10, 5-12,
13 <https://doi.org/10.1289/ehp.94102s105>, 1994.

14 Hu, W. W., Hu, M., Hu, W., Jimenez, J. L., Yuan, B., Chen, W. T., Wang, M., Wu, Y. S., Chen, C.,
15 Wang, Z. B., Peng, J. F., Zeng, L. M., and Shao, M.: Chemical composition, sources, and aging
16 process of submicron aerosols in Beijing: Contrast between summer and winter, *J. Geophys. Res.*
17 *Atmos.*, 121, 1955-1977, <https://doi.org/10.1002/2015JD024020>, 2016.

18 Jimenez, J. L., Jayne, J. T., Shi, Q., Kolb, C. E., Worsnop, D. R., Yourshaw, I., Seinfeld, J. H.,
19 Flagan, R. C., Zhang, X., Smith, K. A., Morris, J. W., and Davidovits, P.: Ambient aerosol sampling
20 using the Aerodyne Aerosol Mass Spectrometer, *J. Geophys. Res. Atmos.*, 108,
21 <https://doi.org/10.1029/2001JD001213>, 2003.

22 Jimenez, J. L., Canagaratna, M. R., Donahue, N. M., Prevot, A. S. H., Zhang, Q., Kroll, J. H.,
23 DeCarlo, P. F., Allan, J. D., Coe, H., Ng, N. L., Aiken, A. C., Docherty, K. S., Ulbrich, I. M.,
24 Grieshop, A. P., Robinson, A. L., Duplissy, J., Smith, J. D., Wilson, K. R., Lanz, V. A., Hueglin, C.,
25 Sun, Y. L., Tian, J., Laaksonen, A., Raatikainen, T., Rautiainen, J., Vaattovaara, P., Ehn, M.,
26 Kulmala, M., Tomlinson, J. M., Collins, D. R., Cubison, M. J., Dunlea, E. J., Huffman, J. A., Onasch,
27 T. B., Alfarra, M. R., Williams, P. I., Bower, K., Kondo, Y., Schneider, J., Drewnick, F., Borrmann,
28 S., Weimer, S., Demerjian, K., Salcedo, D., Cottrell, L., Griffin, R., Takami, A., Miyoshi, T.,
29 Hatakeyama, S., Shimono, A., Sun, J. Y., Zhang, Y. M., Dzepina, K., Kimmel, J. R., Sueper, D.,
30 Jayne, J. T., Herndon, S. C., Trimborn, A. M., Williams, L. R., Wood, E. C., Middlebrook, A. M.,
31 Kolb, C. E., Baltensperger, U., and Worsnop, D. R.: Evolution of Organic Aerosols in the
32 Atmosphere, *Science*, 326, 1525-1529, <https://doi.org/10.1126/science.1180353>, 2009.

33 Junninen, H., Ehn, M., Petäjä, T., Luosujärvi, L., Kotiaho, T., Kostianen, R., Rohner, U., Gonin, M.,
34 Fuhrer, K., Kulmala, M., and Worsnop, D. R.: A high-resolution mass spectrometer to measure
35 atmospheric ion composition, *Atmos. Meas. Tech.*, 3, 1039-1053, [https://doi.org/10.5194/amt-3-1039-](https://doi.org/10.5194/amt-3-1039-2010)
36 [2010](https://doi.org/10.5194/amt-3-1039-2010), 2010.

37 Kelly, F. J., and Fussell, J. C.: Size, source and chemical composition as determinants of toxicity
38 attributable to ambient particulate matter, *Atmos. Environ.*, 60, 504-526,
39 <https://doi.org/10.1016/j.atmosenv.2012.06.039>, 2012.

40 Kelly, J. M., Doherty, R. M., O'Connor, F. M., and Mann, G. W.: The impact of biogenic,
41 anthropogenic, and biomass burning volatile organic compound emissions on regional and seasonal
42 variations in secondary organic aerosol, *Atmos. Chem. Phys.*, 18, 7393-7422,
43 <https://doi.org/10.5194/acp-18-7393-2018>, 2018.

44 Kiendler-Scharr, A., Mensah, A. A., Friese, E., Topping, D., Nemitz, E., Prevot, A. S. H., Aijala, M.,
45 Allan, J., Canonaco, F., Canagaratna, M., Carbone, S., Crippa, M., Dall'Osto, M., Day, D. A., De
46 Carlo, P., Di Marco, C. F., Elbern, H., Eriksson, A., Freney, E., Hao, L., Herrmann, H., Hildebrandt,
47 L., Hillamo, R., Jimenez, J. L., Laaksonen, A., McFiggans, G., Mohr, C., O'Dowd, C., Otjes, R.,
48 Ovadnevaite, J., Pandis, S. N., Poulain, L., Schlag, P., Sellegri, K., Swietlicki, E., Tiitta, P.,
49 Vermeulen, A., Wahner, A., Worsnop, D., and Wu, H. C.: Ubiquity of organic nitrates from nighttime
50 chemistry in the European submicron aerosol, *Geophys. Res. Lett.*, 43, 7735-7744,
51 <https://doi.org/10.1002/2016gl069239>, 2016.

52 Kumar, V., Giannoukos, S., Haslett, S. L., Tong, Y., Singh, A., Bertrand, A., Lee, C. P., Wang, D. S.,
53 Bhattu, D., Stefanelli, G., Dave, J. S., Puthussery, J. V., Qi, L., Vats, P., Rai, P., Casotto, R., Satish,
54 R., Mishra, S., Pospisilova, V., Mohr, C., Bell, D. M., Ganguly, D., Verma, V., Rastogi, N.,
55 Baltensperger, U., Tripathi, S. N., Prévôt, A. S. H., and Slowik, J. G.: Real-time chemical speciation

1 and source apportionment of organic aerosol components in Delhi, India, using extractive electrospray
2 ionization mass spectrometry, *Atmos. Chem. Phys. Discuss.*, 2021, 1-35, [https://doi.org/10.5194/acp-](https://doi.org/10.5194/acp-2021-1033)
3 [2021-1033](https://doi.org/10.5194/acp-2021-1033), 2021.

4 Laden, F., Schwartz, J., Speizer, F. E., and Dockery, D. W.: Reduction in fine particulate air pollution
5 and mortality - Extended follow-up of the Harvard six cities study, *Am. J. Respir. Crit. Care Med.*,
6 173, 667-672, <https://doi.org/10.1164/rccm.200503-443OC>, 2006.

7 Lanz, V. A., Alfarra, M. R., Baltensperger, U., Buchmann, B., Hueglin, C., and Prévôt, A. S. H.:
8 Source apportionment of submicron organic aerosols at an urban site by factor analytical modelling of
9 aerosol mass spectra, *Atmos. Chem. Phys.*, 7, 1503-1522, <https://doi.org/10.5194/acp-7-1503-2007>,
10 2007.

11 Lee, B. H., D'Ambro, E. L., Lopez-Hilfiker, F. D., Schobesberger, S., Mohr, C., Zawadowicz, M. A.,
12 Liu, J., Shilling, J. E., Hu, W., Palm, B. B., Jimenez, J. L., Hao, L., Virtanen, A., Zhang, H.,
13 Goldstein, A. H., Pye, H. O. T., and Thornton, J. A.: Resolving Ambient Organic Aerosol Formation
14 and Aging Pathways with Simultaneous Molecular Composition and Volatility Observations, *ACS*
15 *Earth Space Chem*, 4, 391-402, [10.1021/acsearthspacechem.9b00302](https://doi.org/10.1021/acsearthspacechem.9b00302), 2020.

16 Li, N., Sioutas, C., Cho, A., Schmitz, D., Misra, C., Sempff, J., Wang, M. Y., Oberley, T., Froines, J.,
17 and Nel, A.: Ultrafine particulate pollutants induce oxidative stress and mitochondrial damage,
18 *Environ Health Perspect*, 111, 455-460, <https://doi.org/10.1289/ehp.6000>, 2003.

19 Lohmann, U., and Feichter, J.: Global indirect aerosol effects: a review, *Atmos. Chem. Phys.*, 5, 715-
20 737, <https://doi.org/10.5194/acp-5-715-2005>, 2005.

21 Lopez-Hilfiker, F. D., Mohr, C., Ehn, M., Rubach, F., Kleist, E., Wildt, J., Mentel, T. F., Lutz, A.,
22 Hallquist, M., Worsnop, D., and Thornton, J. A.: A novel method for online analysis of gas and
23 particle composition: description and evaluation of a Filter Inlet for Gases and AEROSols
24 (FIGAERO), *Atmos. Meas. Tech.*, 7, 983-1001, <https://doi.org/10.5194/amt-7-983-2014>, 2014.

25 Lopez-Hilfiker, F. D., Iyer, S., Mohr, C., Lee, B. H., D'Ambro, E. L., Kurtén, T., and Thornton, J. A.:
26 Constraining the sensitivity of iodide adduct chemical ionization mass spectrometry to multifunctional
27 organic molecules using the collision limit and thermodynamic stability of iodide ion adducts, *Atmos.*
28 *Meas. Tech.*, 9, 1505-1512, <https://doi.org/10.5194/amt-9-1505-2016>, 2016.

29 Lopez-Hilfiker, F. D., Pospisilova, V., Huang, W., Kalberer, M., Mohr, C., Stefenelli, G., Thornton, J.
30 A., Baltensperger, U., Prevot, A. S. H., and Slowik, J. G.: An extractive electrospray ionization time-
31 of-flight mass spectrometer (EESI-TOF) for online measurement of atmospheric aerosol particles,
32 *Atmos. Meas. Tech.*, 12, 4867-4886, <https://doi.org/10.5194/amt-12-4867-2019>, 2019.

33 Mayer, H.: Air pollution in cities, *Atmos. Environ.*, 33, 4029-4037, [https://doi.org/10.1016/S1352-](https://doi.org/10.1016/S1352-2310(99)00144-2)
34 [2310\(99\)00144-2](https://doi.org/10.1016/S1352-2310(99)00144-2), 1999.

35 Middlebrook, A. M., Bahreini, R., Jimenez, J. L., and Canagaratna, M. R.: Evaluation of
36 Composition-Dependent Collection Efficiencies for the Aerodyne Aerosol Mass Spectrometer using
37 Field Data, *Aerosol Sci. Technol.*, 46, 258-271, <https://doi.org/10.1080/02786826.2011.620041>, 2012.

38 Mohr, C., DeCarlo, P. F., Heringa, M. F., Chirico, R., Slowik, J. G., Richter, R., Reche, C., Alastuey,
39 A., Querol, X., Seco, R., Penuelas, J., Jimenez, J. L., Crippa, M., Zimmermann, R., Baltensperger, U.,
40 and Prevot, A. S. H.: Identification and quantification of organic aerosol from cooking and other
41 sources in Barcelona using aerosol mass spectrometer data, *Atmos. Chem. Phys.*, 12, 1649-1665,
42 <https://doi.org/10.5194/acp-12-1649-2012>, 2012.

43 Myhre, G., Shindell, D., and Pongratz, J.: Anthropogenic and natural radiative forcing, 2014.

44 Ng, N. L., Canagaratna, M. R., Jimenez, J. L., Chhabra, P. S., Seinfeld, J. H., and Worsnop, D. R.:
45 Changes in organic aerosol composition with aging inferred from aerosol mass spectra, *Atmos. Chem.*
46 *Phys.*, 11, 6465-6474, <https://doi.org/10.5194/acp-11-6465-2011>, 2011a.

47 Ng, N. L., Canagaratna, M. R., Jimenez, J. L., Zhang, Q., Ulbrich, I. M., and Worsnop, D. R.: Real-
48 Time Methods for Estimating Organic Component Mass Concentrations from Aerosol Mass
49 Spectrometer Data, *Environ. Sci. Technol.*, 45, 910-916, <https://doi.org/10.1021/es102951k>, 2011b.

50 Paatero, P., and Tapper, U.: Positive matrix factorization: A non-negative factor model with optimal
51 utilization of error estimates of data values, *Environmetrics*, 5, 111-126,
52 <https://doi.org/10.1002/env.3170050203>, 1994.

53 Paatero, P.: The Multilinear Engine—A Table-Driven, Least Squares Program for Solving Multilinear
54 Problems, Including the n-Way Parallel Factor Analysis Model, *J. Comput. Graph. Stat.*, 8, 854-888,
55 <https://doi.org/10.1080/10618600.1999.10474853>, 1999.

1 Paatero, P., and Hopke, P. K.: Discarding or downweighting high-noise variables in factor analytic
2 models, *Anal. Chim. Acta*, 490, 277-289, [https://doi.org/10.1016/S0003-2670\(02\)01643-4](https://doi.org/10.1016/S0003-2670(02)01643-4), 2003.

3 Paatero, P., Eberly, S., Brown, S. G., and Norris, G. A.: Methods for estimating uncertainty in factor
4 analytic solutions, *Atmos. Meas. Tech.*, 7, 781-797, <https://doi.org/10.5194/amt-7-781-2014>, 2014.

5 Penner, J. E., Xu, L., and Wang, M. H.: Satellite methods underestimate indirect climate forcing by
6 aerosols, *Proc Natl Acad Sci U S A*, 108, 13404-13408, <https://doi.org/10.1073/pnas.1018526108>,
7 2011.

8 Pieber, S. M., El Haddad, I., Slowik, J. G., Canagaratna, M. R., Jayne, J. T., Platt, S. M., Bozzetti, C.,
9 Daellenbach, K. R., Frohlich, R., Vlachou, A., Klein, F., Dommen, J., Miljevic, B., Jimenez, J. L.,
10 Worsnop, D. R., Baltensperger, U., and Prevot, A. S. H.: Inorganic Salt Interference on CO₂⁺ in
11 Aerodyne AMS and ACSM Organic Aerosol Composition Studies, *Environ. Sci. Technol.*, 50, 10494-
12 10503, <https://doi.org/10.1021/acs.est.6b01035>, 2016.

13 Pope, C. A., Burnett, R. T., Thun, M. J., Calle, E. E., Krewski, D., Ito, K., and Thurston, G. D.: Lung
14 cancer, cardiopulmonary mortality, and long-term exposure to fine particulate air pollution, *JAMA*,
15 287, 1132-1141, <https://doi.org/10.1001/jama.287.9.1132>, 2002.

16 Qi, L., Chen, M. D., Stefenelli, G., Pospisilova, V., Tong, Y. D., Bertrand, A., Hueglin, C., Ge, X. L.,
17 Baltensperger, U., Prevot, A. S. H., and Slowik, J. G.: Organic aerosol source apportionment in
18 Zurich using an extractive electrospray ionization time-of-flight mass spectrometer (EESI-TOF-MS) -
19 Part 2: Biomass burning influences in winter, *Atmos. Chem. Phys.*, 19, 8037-8062,
20 <https://doi.org/10.5194/acp-19-8037-2019>, 2019.

21 Qi, L., Vogel, A. L., Esmaeilirad, S., Cao, L., Zheng, J., Jaffrezo, J. L., Fermo, P., Kasper-Giebl, A.,
22 Daellenbach, K. R., Chen, M., Ge, X., Baltensperger, U., Prévôt, A. S. H., and Slowik, J. G.: A 1-year
23 characterization of organic aerosol composition and sources using an extractive electrospray
24 ionization time-of-flight mass spectrometer (EESI-TOF), *Atmos. Chem. Phys.*, 20, 7875-7893,
25 <https://doi.org/10.5194/acp-20-7875-2020>, 2020.

26 Reuter, S., Gupta, S. C., Chaturvedi, M. M., and Aggarwal, B. B.: Oxidative stress, inflammation, and
27 cancer How are they linked?, *Free Radic. Biol. Med.*, 49, 1603-1616,
28 <https://doi.org/10.1016/j.freeradbiomed.2010.09.006>, 2010.

29 Rouvière, A., Brulfert, G., Baussand, P., and Chollet, J.-P.: Monoterpene source emissions from
30 Chamonix in the Alpine Valleys, *Atmospheric Environment*, 40, 3613-3620,
31 <https://doi.org/10.1016/j.atmosenv.2005.09.058>, 2006.

32 Slowik, J. G., Vlasenko, A., McGuire, M., Evans, G. J., and Abbatt, J. P. D.: Simultaneous factor
33 analysis of organic particle and gas mass spectra: AMS and PTR-MS measurements at an urban site,
34 *Atmos. Chem. Phys.*, 10, 1969-1988, <https://doi.org/10.5194/acp-10-1969-2010>, 2010.

35 Stefenelli, G., Pospisilova, V., Lopez-Hilfiker, F. D., Daellenbach, K. R., Hüglin, C., Tong, Y.,
36 Baltensperger, U., Prévôt, A. S. H., and Slowik, J. G.: Organic aerosol source apportionment in
37 Zurich using an extractive electrospray ionization time-of-flight mass spectrometer (EESI-TOF-MS) –
38 Part 1: Biogenic influences and day–night chemistry in summer, *Atmos. Chem. Phys.*, 19, 14825-
39 14848, <https://doi.org/10.5194/acp-19-14825-2019>, 2019.

40 Struckmeier, C., Drewnick, F., Fachinger, F., Gobbi, G. P., and Borrmann, S.: Atmospheric aerosols
41 in Rome, Italy: sources, dynamics and spatial variations during two seasons, *Atmos. Chem. Phys.*, 16,
42 15277-15299, <https://doi.org/10.5194/acp-16-15277-2016>, 2016.

43 Sun, Y. L., Zhang, Q., Schwab, J. J., Demerjian, K. L., Chen, W. N., Bae, M. S., Hung, H. M.,
44 Hogrefe, O., Frank, B., Rattigan, O. V., and Lin, Y. C.: Characterization of the sources and processes
45 of organic and inorganic aerosols in New York city with a high-resolution time-of-flight aerosol mass
46 spectrometer, *Atmos. Chem. Phys.*, 11, 1581-1602, <https://doi.org/10.5194/acp-11-1581-2011>, 2011.

47 Sun, Y. L., Wang, Z. F., Fu, P. Q., Yang, T., Jiang, Q., Dong, H. B., Li, J., and Jia, J. J.: Aerosol
48 composition, sources and processes during wintertime in Beijing, China, *Atmos. Chem. Phys.*, 13,
49 4577-4592, <https://doi.org/10.5194/acp-13-4577-2013>, 2013.

50 Sun, Y. L., Du, W., Fu, P. Q., Wang, Q. Q., Li, J., Ge, X. L., Zhang, Q., Zhu, C. M., Ren, L. J., Xu,
51 W. Q., Zhao, J., Han, T. T., Worsnop, D. R., and Wang, Z. F.: Primary and secondary aerosols in
52 Beijing in winter: sources, variations and processes, *Atmos. Chem. Phys.*, 16, 8309-8329,
53 <https://doi.org/10.5194/acp-16-8309-2016>, 2016a.

54 Sun, Y. L., Wang, Z. F., Wild, O., Xu, W. Q., Chen, C., Fu, P. Q., Du, W., Zhou, L. B., Zhang, Q.,
55 Han, T. T., Wang, Q. Q., Pan, X. L., Zheng, H. T., Li, J., Guo, X. F., Liu, J. G., and Worsnop, D. R.:

1 "APEC Blue": Secondary Aerosol Reductions from Emission Controls in Beijing, *Sci. Rep.*, 6, 20668,
2 <https://doi.org/10.1038/srep20668> (2016), 2016b.

3 Talhout, R., Opperhuizen, A., and van Amsterdam, J. G. C.: Sugars as tobacco ingredient: Effects on
4 mainstream smoke composition, *Food Chem. Toxicol.*, 44, 1789-1798,
5 <https://doi.org/10.1016/j.fct.2006.06.016>, 2006.

6 Tong, Y., Pospisilova, V., Qi, L., Duan, J., Gu, Y., Kumar, V., Rai, P., Stefenelli, G., Wang, L.,
7 Wang, Y., Zhong, H., Baltensperger, U., Cao, J., Huang, R. J., Prévôt, A. S. H., and Slowik, J. G.:
8 Quantification of solid fuel combustion and aqueous chemistry contributions to secondary organic
9 aerosol during wintertime haze events in Beijing, *Atmos. Chem. Phys.*, 21, 9859-9886,
10 <https://doi.org/10.5194/acp-21-9859-2021>, 2021.

11 Ulbrich, I. M., Canagaratna, M. R., Zhang, Q., Worsnop, D. R., and Jimenez, J. L.: Interpretation of
12 organic components from Positive Matrix Factorization of aerosol mass spectrometric data, *Atmos.*
13 *Chem. Phys.*, 9, 2891-2918, <https://doi.org/10.5194/acp-9-2891-2009>, 2009.

14 Vlachou, A., Tobler, A., Lamkaddam, H., Canonaco, F., Daellenbach, K. R., Jaffrezo, J. L.,
15 Minguillon, M. C., Maasikmets, M., Teinmaa, E., Baltensperger, U., El Haddad, I., and Prevot, A. S.
16 H.: Development of a versatile source apportionment analysis based on positive matrix factorization:
17 a case study of the seasonal variation of organic aerosol sources in Estonia, *Atmos. Chem. Phys.*, 19,
18 7279-7295, <https://doi.org/10.5194/acp-19-7279-2019>, 2019.

19 Wang, D. S., Lee, C. P., Krechmer, J. E., Majluf, F., Tong, Y., Canagaratna, M. R., Schmale, J.,
20 Prévôt, A. S. H., Baltensperger, U., Dommen, J., El Haddad, I., Slowik, J. G., and Bell, D. M.:
21 Constraining the response factors of an extractive electrospray ionization mass spectrometer for near-
22 molecular aerosol speciation, *Atmos. Meas. Tech.*, 14, 6955-6972, [https://doi.org/10.5194/amt-14-](https://doi.org/10.5194/amt-14-6955-2021)
23 [6955-2021](https://doi.org/10.5194/amt-14-6955-2021), 2021.

24 Xu, L., Suresh, S., Guo, H., Weber, R. J., and Ng, N. L.: Aerosol characterization over the
25 southeastern United States using high-resolution aerosol mass spectrometry: spatial and seasonal
26 variation of aerosol composition and sources with a focus on organic nitrates, *Atmos. Chem. Phys.*,
27 15, 7307-7336, <https://doi.org/10.5194/acp-15-7307-2015>, 2015.

28 Xu, W. Q., Sun, Y. L., Wang, Q. Q., Zhao, J., Wang, J. F., Ge, X. L., Xie, C. H., Zhou, W., Du, W.,
29 Li, J., Fu, P. Q., Wang, Z. F., Worsnop, D. R., and Coe, H.: Changes in Aerosol Chemistry From 2014
30 to 2016 in Winter in Beijing: Insights From High-Resolution Aerosol Mass Spectrometry, *J. Geophys.*
31 *Res. Atmos.*, 124, 1132-1147, <https://doi.org/10.1029/2018JD029245>, 2019.

32 Zhang, H., Yee, L. D., Lee, B. H., Curtis, M. P., Worton, D. R., Isaacman-VanWertz, G., Offenberg,
33 J. H., Lewandowski, M., Kleindienst, T. E., Beaver, M. R., Holder, A. L., Lonneman, W. A.,
34 Docherty, K. S., Jaoui, M., Pye, H. O. T., Hu, W., Day, D. A., Campuzano-Jost, P., Jimenez, J. L.,
35 Guo, H., Weber, R. J., de Gouw, J., Koss, A. R., Edgerton, E. S., Brune, W., Mohr, C., Lopez-
36 Hilfiker, F. D., Lutz, A., Kreisberg, N. M., Spielman, S. R., Hering, S. V., Wilson, K. R., Thornton, J.
37 A., and Goldstein, A. H.: Monoterpenes are the largest source of summertime organic aerosol in the
38 southeastern United States, *Proc Natl Acad Sci U S A*, 115, 2038,
39 <https://doi.org/10.1073/pnas.1717513115>, 2018.

40 Zhang, J. K., Sun, Y., Liu, Z. R., Ji, D. S., Hu, B., Liu, Q., and Wang, Y. S.: Characterization of
41 submicron aerosols during a month of serious pollution in Beijing, 2013, *Atmos. Chem. Phys.*, 14,
42 2887-2903, <https://doi.org/10.5194/acp-14-2887-2014>, 2014.

43 Zhang, Q., Worsnop, D. R., Canagaratna, M. R., and Jimenez, J. L.: Hydrocarbon-like and
44 oxygenated organic aerosols in Pittsburgh: insights into sources and processes of organic aerosols,
45 *Atmos. Chem. Phys.*, 5, 3289-3311, <https://doi.org/10.5194/acp-5-3289-2005>, 2005.

46 Zhang, Q., Jimenez, J. L., Canagaratna, M. R., Ulbrich, I. M., Ng, N. L., Worsnop, D. R., and Sun, Y.
47 L.: Understanding atmospheric organic aerosols via factor analysis of aerosol mass spectrometry: a
48 review, *Anal. Bioanal. Chem.*, 401, 3045-3067, <https://doi.org/10.1007/s00216-011-5355-y>, 2011.

49 Zhang, Y. X., Schauer, J. J., Zhang, Y. H., Zeng, L. M., Wei, Y. J., Liu, Y., and Shao, M.:
50 Characteristics of particulate carbon emissions from real-world Chinese coal combustion, *Environ.*
51 *Sci. Technol.*, 42, 5068-5073, <https://doi.org/10.1021/es7022576>, 2008.

52 Zhao, J., Qiu, Y. M., Zhou, W., Xu, W. Q., Wang, J. F., Zhang, Y. J., Li, L. J., Xie, C. H., Wang, Q.
53 Q., Du, W., Worsnop, D. R., Canagaratna, M. R., Zhou, L. B., Ge, X. L., Fu, P. Q., Li, J., Wang, Z.
54 F., Donahue, N. M., and Sun, Y. L.: Organic Aerosol Processing During Winter Severe Haze

1 Episodes in Beijing, *J. Geophys. Res. Atmos.*, 124, 10248-10263,
2 <https://doi.org/10.1029/2019JD030832>, 2019.
3 Zhou, J., Zotter, P., Bruns, E. A., Stefenelli, G., Bhattu, D., Brown, S., Bertrand, A., Marchand, N.,
4 Lamkaddam, H., Slowik, J. G., Prévôt, A. S. H., Baltensperger, U., Nussbaumer, T., El-Haddad, I.,
5 and Dommen, J.: Particle-bound reactive oxygen species (PB-ROS) emissions and formation
6 pathways in residential wood smoke under different combustion and aging conditions, *Atmos. Chem.*
7 *Phys.*, 18, 6985-7000, <https://doi.org/10.5194/acp-18-6985-2018>, 2018.

8